Predicting thermal performance of an enhanced geothermal system from tracer tests in a data assimilation framework

Wu Hui[1], Fu Pengcheng[1], Hawkins Adam Jacob[2], Tang Hewei[1], and Morris Joseph P.[3]

[1]Lawrence Livermore National Laboratory
[2]Cornell University
[3]Lawrence Livermore National Laboratory (DOE)

November 15, 2022

Abstract

Predicting the thermal performance of an enhanced geothermal system (EGS) requires a comprehensive characterization of the underlying fracture flow patterns from practically available data such as tracer data. However, due to the inherent complexities of subsurface fractures and the generally insufficient geological/geophysical data, interpreting tracer data for fracture flow characterization and thermal prediction remains a challenging task. The present study aims to tackle the challenge by leveraging a data assimilation method to maximize the utilization of information inherently contained in tracer data, and meanwhile maintain the flexibility to handle various uncertainties. A tracer data interpretation framework was proposed with the following three components integrated: 1) We use principal component analysis (PCA) to reduce the dimensionality of model parameter space. 2) We use ES-MDA (ensemble smoother with multiple data assimilation) to invert for fracture aperture/flow fields and obtain posterior model ensembles for uncertainty quantification. Various data types are assimilated jointly to improve the predictive ability of the posterior ensemble. 3) The inverted fracture aperture fields are then incorporated into reservoir models to predict thermal performance. We developed a field-scale EGS model to verify the ability of the framework to characterize highly heterogeneous fracture aperture/flow fields and predicting thermal performance. We also applied the framework to a meso-scale field experiment to demonstrate its potential application in real-world geothermal reservoirs. The results indicate that the proposed framework can effectively retrieve fracture flow information from tracer data for thermal prediction and uncertainty quantification, and thus provide informative guidance for EGS optimization and risk management.

1

Predicting thermal performance of an enhanced geothermal system from tracer tests in a data assimilation framework

Hui Wu[1], Pengcheng Fu[1], Adam J. Hawkins[2], Hewei Tang[1], Joseph P. Morris[1]

[1]Atmospheric, Earth, and Energy Division, Lawrence Livermore National Laboratory, Livermore, CA, USA.

[2]Robert Fredrick Smith School of Chemical and Biomolecular Engineering, Cornell University, Ithaca, NY, USA.

Corresponding author: Hui Wu (wu40@llnl.gov)

Key Points:

- Proposed a data assimilation framework to predict thermal performance of enhanced geothermal system (EGS) from tracer data.

- Demonstrated the efficacy of the framework through a synthetic field-scale EGS model and a meso-scale field test.

- Combining conservative and sorptive tracer data offers more accurate prediction of thermal performance than individual tracer.

Abstract

Predicting the thermal performance of an enhanced geothermal system (EGS) requires a comprehensive characterization of the underlying fracture flow patterns from practically available data such as tracer data. However, due to the inherent complexities of subsurface fractures and the generally insufficient geological/geophysical data, interpreting tracer data for fracture flow characterization and thermal prediction remains a challenging task. The present study aims to tackle the challenge by leveraging a data assimilation method to maximize the utilization of information inherently contained in tracer data, and meanwhile maintain the flexibility to handle various uncertainties. A tracer data interpretation framework was proposed with the following three components integrated: 1) We use principal component analysis (PCA) to reduce the dimensionality of model parameter space. 2) We use ES-MDA (ensemble smoother with multiple data assimilation) to invert for fracture aperture/flow fields and obtain posterior model ensembles for uncertainty quantification. Various data types are assimilated jointly to improve the predictive ability of the posterior ensemble. 3) The inverted fracture aperture fields are then incorporated into reservoir models to predict thermal performance. We developed a field-scale EGS model to verify the ability of the framework to characterize highly heterogeneous fracture aperture/flow fields and predicting thermal performance. We also applied the framework to a meso-scale field experiment to demonstrate its potential application in real-world geothermal reservoirs. The results indicate that the proposed framework can effectively retrieve fracture flow information from tracer data for thermal prediction and uncertainty quantification, and thus provide informative guidance for EGS optimization and risk management.

1 Introduction

A wider deployment of geothermal energy, particularly enhanced geothermal systems (EGS), is considered an essential component of the global effort to combat climate change and environment pollution. The optimization and risk management of EGS require accurate predictions of long-term thermal performance under different stimulation and operation scenarios. As EGS relies on natural and/or artificial fractures for fluid circulation and heat extraction, its thermal performance highly depends on fracture flow characteristics (Fox et al., 2015; Fu et al., 2016; Guo et al., 2016b; Chen and Zhao, 2020). Direct observations and measurements of fractures in an EGS setting that is generally several kilometers below the ground surface are extremely difficult. Remarkable effort has been devoted to investigating indirect hydraulic and geophysical testing methods, such as hydraulic and tracer testing, seismic and electrical methods, ground penetrating radar, etc. (Berkowitz, 2002; Neuman, 2005; Maxwell et al., 2010; Wu et al., 2019). Among these methods, tracer testing is a powerful and widely used approach for subsurface fracture characterization (Sanjuan et al., 2006; Brown et al., 2012; Juliusson and Horne, 2013; Hawkins et al., 2018). By injecting tracer-carrying fluid into one or more target fractures and monitoring tracer concentrations at outlet wells, one can obtain tracer breakthrough curves which are expected to reflect fracture flow characteristics.

Interpreting tracer data for fracture flow characterization and thermal performance prediction of an EGS is challenging. Some methods have been developed to directly predict hydrothermal systems' thermal performance from tracer data, but those are inapplicable to EGS due to a significant difference between the two types of geothermal systems. For hydrothermal reservoirs, the porous medium serves as the reservoir for both the fluid mass ("hydro reservoir")

63 and heat ("thermal reservoir"). For an EGS, the hydro reservoir is mainly the fracture apertures
64 whereas the thermal reservoir is the rock body surrounding the fractures. This discrepancy makes
65 directly connecting tracer data to thermal performance extremely challenging. Shook (2001)
66 developed a transformation method to derive a thermal breakthrough curve from a tracer
67 breakthrough curve by utilizing the analogies between governing equations for tracer and heat
68 transport, but the method is only applicable to hydrothermal reservoirs. Guo et al. (2016a)
69 attempted to correlate the metrics of tracer breakthrough curves, including peak concentration
70 and mean residence time, to the life span of an EGS, but the obtained correlations were poor.
71 Traditional temporal moment analysis on tracer breakthrough curves can estimate important
72 fracture characteristics such as fracture volume swept by tracer (Shook, 2003; Wu et al., 2008;
73 Ayling et al., 2016; Hawkins et al., 2017b; Tian et al., 2016; Kittilä et al., 2019). However,
74 fracture volume alone is unable to predict EGS thermal performance because heat extraction
75 from an EGS depends largely on the effective heat exchange area, which cannot be directly
76 calculated through conventional tracer test analysis.

77   A promising strategy is to use inversion-based tracer data interpretation to first
78 characterize fracture aperture/flow fields and then predict EGS thermal performance based on the
79 inversion results. A practical challenge for such inversion problems is that available geological
80 and geophysical data are generally insufficient for constraining the many inherent complexities
81 of subsurface fractures. Some previous studies assumed simplistic fracture models (e.g.,
82 homogeneous fracture aperture, fixed shape) to circumvent these complexities, and used
83 analytical solutions to invert for key parameters such as aperture and heat exchange area (Radilla
84 et al., 2012; Shook and Suzuki, 2017; Hawkins et al., 2018; Suzuki et al., 2019). Such simplified
85 approaches, while efficient and easy to implement, may not be able to capture the complex
86 fracture features necessary for thermal prediction, such as highly heterogeneous aperture
87 distribution. An alternative is to develop a fracture model that properly accounts for the
88 complexities and then use high-fidelity numerical simulations for tracer data inversion. The high-
89 dimensional parameter space of the complex fracture model inevitably leads to an ill-posed
90 inversion problem. Inversion approaches that can handle the equifinality of such problems are
91 therefore desired to find multiple viable realizations to quantify uncertainties in thermal
92 prediction. Commonly used approaches include stochastic modeling (Vogt et al., 2012a; Wu et
93 al., 2021), Markov Chain Monte Carlo (MCMC) (Irving and Singha, 2010; Cui et al., 2011;
94 Vrugt, 2016; Zhang et al., 2018) and ensemble-based data assimilation (Evensen, 1994, 2018;
95 van Leeuwen and Evensen, 1996; Chen and Oliver, 2012; Emerick and Reynolds, 2013; Tang et
96 al., 2021). Compared with stochastic modeling and MCMC, ensemble-based data assimilation is
97 computationally more efficient, and has gained increasing popularity in tracer data interpretation
98 for subsurface characterization (Vogt et al., 2012b; Chen et al., 2013; Crestani et al.,
99 2013; Keller et al., 2018). The result of ensemble-based data assimilation is an ensemble of
100 viable model realizations, each of which can reasonably fit tracer data. The variability among
101 these model realizations represents uncertainties arising from different sources.

102   While important progresses have been made regarding the inversion of
103 aperture/permeability fields from tracer data (Vogt et al., 2012b; Wu et al., 2020; Hawkins et al.,
104 2020), the ability of the inversion results to predict thermal performance requires further
105 investigation. Most of the abovementioned studies focused on aperture/permeability inversion,
106 and only a few discussed the prediction of thermal performance. Vogt et al. (2012b) used an
107 Ensemble Kalman Filter (EnKF) to assimilate conservative tracer data at the Soultz-sous-Forêts
108 EGS reservoir and predicted the thermal performance of the reservoir for 50 years through the

109   inverted reservoir permeability. However, the predictions showed significant uncertainties. Wu
110   et al. (2020) used a stochastic modeling approach to interpreting a conservative tracer test at the
111   EGS Collab field experiment and inferred spatial aperture distribution in a major hydraulic
112   fracture. Multiple satisfactory aperture distributions were obtained, and the predicted thermal
113   responses from these aperture distributions showed considerable uncertainties.

114   In the present study, we propose a tracer data interpretation framework to first invert for
115   spatial distribution of fracture aperture, and then predict thermal performance based on the
116   inversion results. Ensemble smoother with multiple data assimilation (ES-MDA) is employed for
117   tracer data interpretation. We aim to 1) Investigate the efficacy of ensemble-based data
118   assimilation in fracture aperture/permeability inversion from tracer data; 2) Examine the
119   suitability of the inversion results for thermal performance prediction; 3) Explore methods (such
120   as joint data assimilation) to improve prediction accuracy and constrain prediction uncertainties.
121   The novelty of the framework includes the following: 1) While most previous studies only
122   assimilate a single type of data (mainly conservative tracer data as abovementioned), the
123   framework employed here jointly assimilates multiple data types, including conservative and
124   sorptive tracer data, as well as practically available pressure and flow data. The effects of
125   combining different data types are analyzed to provide practical guidance for fracture
126   characterization. 3) The framework integrates fracture aperture inversion with reservoir
127   simulation to allow further investigation of the use of inversion results in thermal performance
128   prediction.

129   The paper is organized as follows. Section 2 describes the main components of the
130   proposed framework. In Section 3, we introduce a synthetic field-scale EGS model to verify the
131   effectiveness of the framework in fracture aperture inversion and thermal performance
132   prediction. Section 4 validates the proposed framework against a meso-scale field experiment at
133   the Altona Field Laboratory (AFL) which involved various tracer tests and a water circulation
134   test. Section 5 provides discussions regarding the capability and limitation of the framework.

2 Tracer data interpretation framework

136   There are three major components in the proposed framework (Fig. 1): 1) Model
137   parameterization and dimensionality reduction; 2) ES-MDA to invert for fracture characteristics

138   from tracer data; and 3) Thermal performance prediction based on the inversion results from ES-
139   MDA. Sections 2.1 to 2.3 describe details of these three components, respectively.
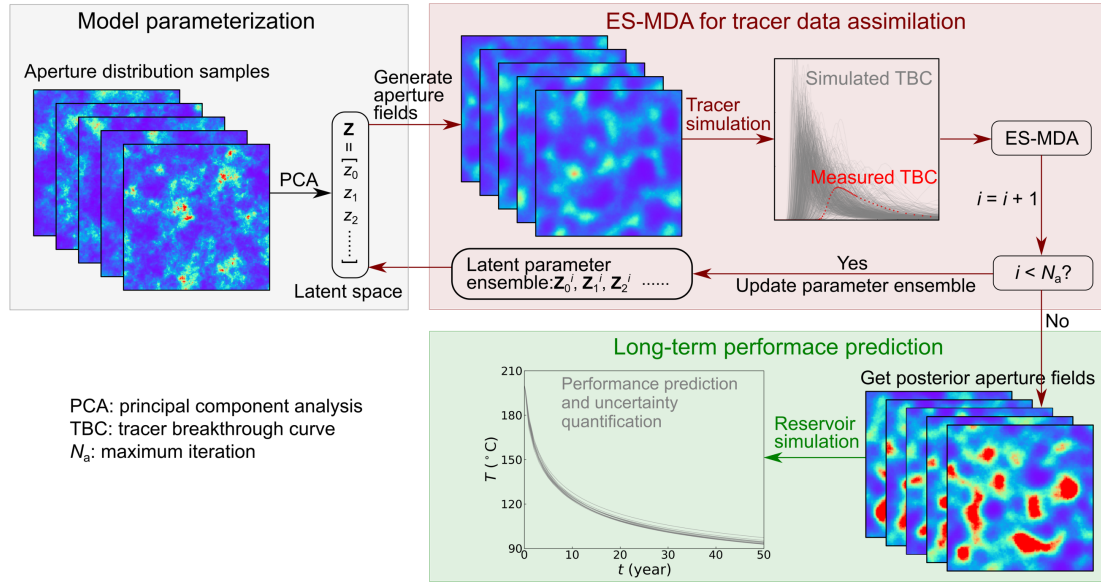

140
141   Fig. 1 Workflow of the tracer data interpretation framework. Aperture distribution within a
142   single, discrete fracture is shown as 2D spatially correlated random fields.

143   2.1 Model parameterization and dimensionality reduction

144   Driven by data scarcity in subsurface characterization problems, we need to parameterize
145   reservoir models with an appropriate level of complexity. The concerned parameter in the
146   present study is the spatial distribution of aperture in a discrete rock fracture, which is usually
147   described by 2D spatially correlated fields (Fig. 1). In real-world problems, fracture aperture is
148   generally highly heterogeneous following Gaussian (Pyrak-Nolte and Morris, 2000; Guo et al.,
149   2016a; Wu et al., 2021) or non-Gaussian distributions (Power and Tullis, 1992). Cell-based
150   parameterization of aperture fields results in a large parameter space, and the auto-correlation of
151   aperture is not naturally honored. To address this issue, the proposed framework employs
152   principal component analysis (PCA) to reduce the dimensionality of the parameter space.

153   PCA is a widely used unsupervised technique to project high-dimensional data to a latent
154   space defined by orthogonal principal components. These principal components can be obtained
155   through either computing the eigenvectors and eigenvalues of the covariance matrix of the
156   original high-dimensional data or directly performing singular value decomposition (SVD) on
157   the original data. The principal components are then ordered in such a way that the higher-ranked
158   principal components preserve greater variance in the original data. By truncating the vector of
159   principal components, the original data can be represented by a low-dimensional latent space
160   while preserving most of the variance or "energy" in the original data. PCA has been widely
161   used to reduce the dimensionality of spatially correlated fields, such as permeability and aperture
162   distribution, in history matching and inversion problems pertaining to subsurface
163   aquifer/reservoir characterization (Sarma et al., 2008; Hawkins et al., 2020). Below we briefly
164   introduce the major steps of PCA through SVD (Liu and Durlofsky, 2020).

- Prior to PCA, we first generate an ensemble of aperture fields (cell-based values)
165
166   according to our prior knowledge from geological/geophysical measurements,

167 such as core logs, wellbore images and outcrop analysis. The generated sample
168 fields, denoted as $\mathbf{M} = [\mathbf{m}_1 \ \mathbf{m}_2 \ \dots \ \mathbf{m}_{N_r}] \in \mathbb{R}^{N_c \times N_r}$, where N_c is the number of
169 unknowns (i.e., the number of discretized cells) in each sample field and N_r is the
170 number of generated sample fields, are provided to PCA as training data. The N_r
171 fields collectively represent the range of variations of the aperture field.

172 • The sample fields are assembled into a matrix $\mathbf{M}_c$ as,

173
$$\mathbf{M}_c = \frac{1}{\sqrt{N_r-1}}\left[\mathbf{m}_1 - \bar{\mathbf{m}} \ \ \mathbf{m}_2 - \bar{\mathbf{m}} \ \dots \ \mathbf{m}_{N_r} - \bar{\mathbf{m}}\right] \qquad (1)$$

174 where $\bar{\mathbf{m}}$ denotes the mean of the N_r sample fields.

175 • SVD is then performed on $\mathbf{M}_c$ to obtain singular values and matrices,

176
$$\mathbf{M}_c = \mathbf{U}\boldsymbol{\Sigma}\mathbf{V}^T \qquad (2)$$
177 where $\mathbf{U} \in \mathbb{R}^{N_c \times N_r}$ and $\mathbf{V} \in \mathbb{R}^{N_r \times N_r}$ are the left and right singular matrices,
178 respectively, and $\boldsymbol{\Sigma} \in \mathbb{R}^{N_r \times N_r}$ is a diagonal matrix with each diagonal element as a
179 singular value.

180 • We then select sub-matrices $\mathbf{U}_l$ and $\boldsymbol{\Sigma}_l$, where $\mathbf{U}_l \in \mathbb{R}^{N_c \times l}$ contains the first l ($l \ll$
181 N_c) columns in $\mathbf{U}$ and $\boldsymbol{\Sigma}_l \in \mathbb{R}^{l \times l}$ is a diagonal matrix containing the first l singular
182 values in $\boldsymbol{\Sigma}$. An original sample field $\mathbf{m}_i$ can be reconstructed from a latent
183 parameter vector $\mathbf{z}_i$ using the following equations,

184
$$\mathbf{z}_i = \boldsymbol{\Sigma}_l^{-1}\mathbf{U}_l^T(\mathbf{m}_i - \bar{\mathbf{m}}) \qquad (3)$$
185
$$\hat{\mathbf{m}}_i = \bar{\mathbf{m}} + \mathbf{U}_l\boldsymbol{\Sigma}_l\mathbf{z}_i \qquad (4)$$
186 where $\hat{\mathbf{m}}_i$ is the reconstructed sample field for $\mathbf{m}_i$.

187 • New sample fields can also be generated from,

188
$$\mathbf{m}(\mathbf{z}) = \bar{\mathbf{m}} + \mathbf{U}_l\boldsymbol{\Sigma}_l\mathbf{z} \qquad (5)$$
189 where $\mathbf{z}$ is a l-dimensional latent parameter vector with each element
190 independently sampled from the standard normal distribution.

191 After dimensionality reduction using PCA, the high-dimensional aperture field $\mathbf{m}$ can be
192 represented by a low-dimensional latent space $\mathbf{z}$. In section 3.3, we demonstrate the
193 reconstruction of an original aperture field from latent space, and also analyze the effect of the
194 dimensionality of $\mathbf{z}$.

195 2.2 ES-MDA for tracer data interpretation

196 The second step in the proposed framework is to invert for latent parameters by
197 assimilating tracer data using ES-MDA. ES-MDA, developed by Emerick and Reynolds (2013),
198 uses an iterative scheme to assimilate historical data multiple times and update model parameters
199 so that model responses match the historical data to a satisfactory level. Compared with other
200 ensemble-based data assimilation methods such as EnKF and Ensemble Smoother (ES), ES-
201 MDA alleviates the computational burden of EnKF by assimilating all historical data
202 simultaneously and addresses the unsatisfactory data matching quality in ES by assimilating the
203 historical data multiple times. The detailed derivation of ES-MDA is described in Emerick and
204 Reynolds (2013), and below we briefly introduce the main procedures of ES-MDA for tracer
205 data interpretation (Fig. 1).

206 • First, a prior ensemble of parameter sets is generated according to the prior
207 distribution of model parameters. In the proposed framework, the prior ensemble
208 of latent parameters, denoted as $\mathbf{Z}^0 = [\mathbf{z}_1^0 \ \mathbf{z}_2^0 \ \ldots \ \mathbf{z}_{N_e}^0] \in \mathbb{R}^{l \times N_e}$ where N_e is the
209 number of parameter sets (ensemble size), can be generated by randomly
210 sampling from the standard normal distribution.

211 • With the prior ensemble, we can generate the corresponding aperture fields
212 through equation (5), denoted as $\mathbf{M}^0 = [\mathbf{m}(\mathbf{z}_1^0) \ \mathbf{m}(\mathbf{z}_2^0) \ \ldots \ \mathbf{m}(\mathbf{z}_{N_e}^0)] \in \mathbb{R}^{N_c \times N_e}$. We
213 then calculate model responses for each aperture field according to forward model
214 $\mathbf{y}_i^0 = f(\mathbf{m}(\mathbf{z}_i^0)) \in \mathbb{R}^{N_d}$, where 0 in the superscript denotes the iteration number. i
215 $= 1, 2, \ldots, N_e$, and N_d is the number of measurements. f and $\mathbf{y}$ denote the forward
216 model and the corresponding model response, respectively. For the analysis of
217 tracer data, f is a tracer simulation model and $\mathbf{y}$ is tracer breakthrough data.

218 • The following equation is then used to update the prior ensemble iteratively,

219 $$\mathbf{z}_i^n = \mathbf{z}_i^{n-1} + \mathbf{C}_{ZY}^{n-1}(\mathbf{C}_{YY}^{n-1} + \alpha_n \mathbf{C}_Y^{n-1})^{-1}(\mathbf{y}_{obs} + \boldsymbol{\epsilon}_i - \mathbf{y}_i^{n-1}) \qquad (6)$$
220 where $n = 1, 2, \ldots, N_a$, denoting the iteration of ES-MDA. N_a is the user-defined
221 data assimilation number. $\mathbf{z}_i^n$ is the updated parameter sets after the current
222 iteration. $\mathbf{C}_{ZY} \in \mathbb{R}^{l \times N_d}$ is the cross-covariance matrix between the current
223 parameter ensemble $\mathbf{Z}^{n-1} = [\mathbf{z}_1^{n-1} \ \mathbf{z}_2^{n-1} \ \ldots \ \mathbf{z}_{N_e}^{n-1}] \in \mathbb{R}^{l \times N_e}$ and the corresponding
224 model responses $\mathbf{y}^{n-1} = [\mathbf{y}_1^{n-1} \ \mathbf{y}_2^{n-1} \ \ldots \ \mathbf{y}_{N_e}^{n-1}] \in \mathbb{R}^{N_d \times N_e}$. $\mathbf{C}_{YY} \in \mathbb{R}^{N_d \times N_d}$ is the
225 auto-covariance matrix of model responses. $\mathbf{C}_Y \in \mathbb{R}^{N_d \times N_d}$ is the covariance
226 matrix of the measurement errors of the historical data being assimilated, i.e., $\mathbf{y}_{obs}$.
227 $\boldsymbol{\epsilon}_i$ is random Gaussian noise drawn from $N(0, \alpha_n \mathbf{C}_Y)$. α_n is the user-defined
228 inflation coefficient at the current iteration. According to Emerick and Reynolds
229 (2013), the following condition should be satisfied,
230 $$\sum_{n=1}^{N_a} \frac{1}{\alpha^n} = 1 \qquad (7)$$

231 After N_a updates, we can obtain the posterior ensemble of parameter sets $\mathbf{Z}^{N_a}$ as well as
232 the corresponding posterior aperture distributions.

233 ## 2.3 Thermal performance prediction

234 Another major component of the proposed framework is a thermal performance
235 prediction module using the obtained posterior ensemble of aperture distributions. We
236 incorporate the posterior aperture distributions into 3D reservoir models and perform simulations
237 to predict long-term thermal performance. The predictions from different aperture distributions
238 in the posterior ensemble represent the prediction uncertainty.

239 **3 Demonstration using a field-scale single-fracture EGS model**

240 In this section, we develop a field-scale EGS model to generate synthetic data to evaluate
241 the effectiveness of the proposed framework in predicting thermal performance. The EGS model
242 involves a dominant horizontal fracture in a large body of low permeability crystalline rock. An
243 injection well and two production wells are drilled into the rock formation and intersect the
244 fracture (Fig. 2). The application of the proposed framework to EGS consisting of multiple or
245 many fractures will be addressed in future work. We perform tracer and thermal simulations to
246 obtain synthetic tracer, pressure, and flow rate data as well as thermal breakthrough curves at the

247   two production wells. The framework in Fig. 1 is then used to predict the thermal breakthrough
248   curves from the tracer, pressure and flow rate data.

249   3.1 Model setup

250   The dimensions of the EGS model are $3000 \times 3000 \times 3000$ m^3 (Fig. 2). The horizontal
251   fracture is located in the center of the model with a size of 800×800 m^2. The square shape of the
252   hypothetical fracture was for convenience. The somewhat unrealistic and idealized geometric
253   shape still fulfills the needs for generating synthetic data and validate the workflow. A vertical
254   temperature gradient of 40 °C/km is assumed in the model with an initial temperature of 140 °C
255   at model top. The temperature at the fracture depth is therefore 200 °C. The fracture is
256   represented by a thin layer of elements $5 \times 5 \times 0.004$ m^3 in size. The mesh resolution of the rock
257   matrix is $5 \times 5 \times 2.5$ m^3 near the fracture and becomes progressively coarser in the far field. The
258   resulting computational domain consists of approximately 2,800,000 elements.

259   To demonstrate the efficacy of the proposed framework, we desire the fracture's aperture
260   to be highly heterogeneous (Fig. 2). We use the following procedure to generate the aperture
261   distribution: 1) We first generate a random 160×160 gaussian field and then transform the
262   gaussian field to a binary facies field: Voxel values smaller than a threshold are reassigned as
263   zero and the others as one. 2) Each facies in the binary field is populated with an independently
264   generated random gaussian fields following a log-normal distribution. The "background" facies,
265   visible as the green-to-red area in Fig. 2 has a mean aperture of 3 mm, a standard deviation of 2
266   mm, and a correlation length of 300 m. The "inclusion" facies, visible as the blue patches, has a
267   mean aperture of 0.6 mm, a standard deviation of 0.4 mm and a correlation length of 500 m.
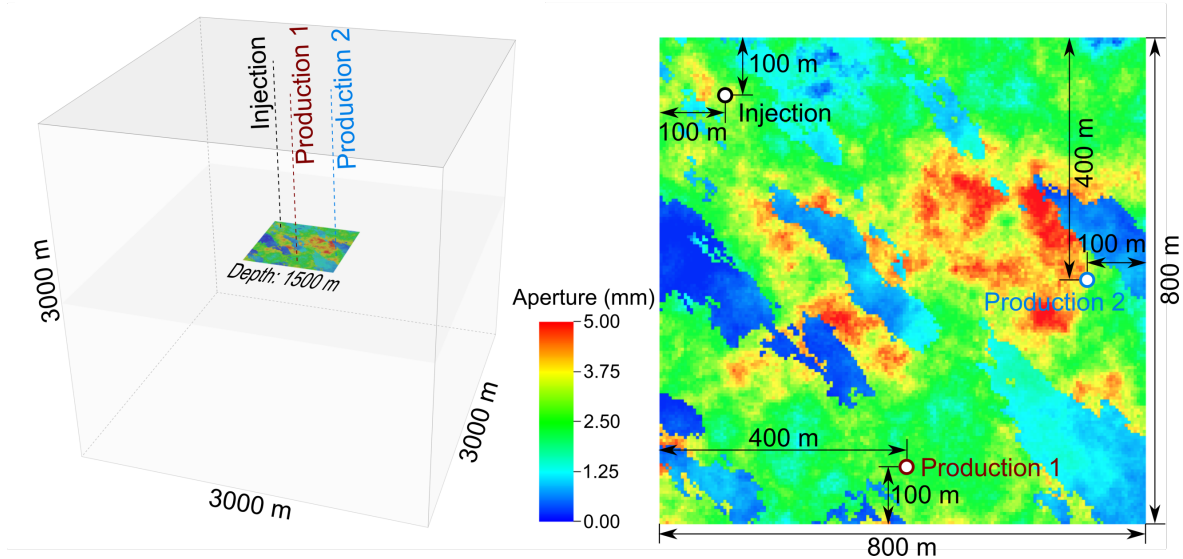

268

269   Fig. 2 A field-scale EGS model with a horizontal fracture connecting an injection and two
270   production wells. Left: Spatial relationship between the simulation domain, the fracture, and the
271   three wells. Right: The spatial distribution of fracture aperture in a plan view.

272   3.2 Tracer and thermal modeling

273   We use GEOS, a massively parallel multi-physics simulation platform developed at the
274   Lawrence Livermore National Laboratory (Settgast et al., 2017), for tracer and thermal modeling

275   in the present study. The tracer transport module in GEOS has been detailed in Guo et al.
276   (2016a) and Wu et al. (2021), and readers are referred to Guo et al. (2016b) for the details of the
277   thermal module in GEOS.

278   For tracer modeling, we include both conservative and sorptive tracers. A hydrostatic
279   initial pressure is assumed in the model with a pressure of 30 MPa at the fracture depth. The
280   injection rate is 10 L/s and we keep constant downhole pressure (30 MPa) at the two production
281   wells. Tracers are injected into the horizontal fracture for one hour and we simulate the tracer
282   transport process for 40 hours to obtain tracer breakthrough curves at the two production wells.
283   Because the fracture is represented by a thin layer of porous media, we calculate the equivalent
284   porosity and permeability of the fracture layer through $\phi = w/H$ and $k = w^3/12H$ respectively
285   (Guo et al., 2016a), where w is the aperture and $H = 4$ mm is the thickness of the fracture grid
286   elements. Other parameters for tracer modeling are listed in Table 1. For sorptive tracer
287   modeling, we assume an equilibrium sorption process with a partition coefficient of 0.3 mm. For
288   a typical matrix diffusion coefficient of 1×10^{-9} m^2/s, we found that the rock formation
289   surrounding the fracture has little effect on the tracer transport process in the fracture. Therefore,
290   we assume that tracer transport is confined to the target fracture and only the horizontal fracture
291   is considered for tracer modeling. Fracture boundaries are assumed impermeable.

292   The simulated tracer breakthrough curves at the two production wells are shown in Fig.
293   3(a). Due to sorption, the breakthrough curves for the sorptive tracer have delayed peaks with
294   smaller peak magnitudes compared with the counterparts for conservative tracer. The simulated
295   pressure difference between the injection and production wells is 2.8 kPa, and the simulated
296   production rates at production wells 1 and 2 are 2.84 and 7.16 L/s respectively. For both
297   conservative and sorptive tracers, tracer breakthrough is earlier and peak magnitude is smaller at
298   production well 1 than at production well 2.

299   For thermal modeling, we circulate water among the injection and production wells with
300   an injection rate of 20 L/s and an injection temperature of 50 °C for 50 years. Similar to tracer
301   modeling, we keep the downhole pressure at 30 MPa at the two production wells. The upper,
302   lower and lateral model boundaries are assumed impermeable to both fluid and heat. This is
303   justified because 1) the rock matrix is largely impermeable, and 2) the cooling front at the end of
304   50 years is still far from the boundary. Parameters for thermal modeling are also summarized in
305   Table 1. We assume constant water viscosity independent of temperature. We do not consider
306   thermo-mechanical coupling in the thermal modeling. As shown in Fig. 3(b), the temperature
307   decrease at production well 1 is slower than that at production well 2 due to the relatively smaller
308   production rate.

309   The tracer breakthrough curves in Fig. 3(a) as well as the pressure and flow rate data are
310   then used as synthetic "measurements" for subsequent ES-MDA to invert for the aperture
311   distribution in the fracture. The goal is to predict the flow rate-averaged production temperature
312   curve in Fig. 3(b) from the posterior aperture distributions obtained from ES-MDA.

313

314

315

316

317
318   Table 1 Parameters for tracer and thermal modeling of the field-scale EGS model.

| Parameter	Value
Porosity of rock matrix	0.01
Permeability of rock matrix (m^2)	1×10^{-16}
Density of rock matrix (kg/m^3)	2500
Specific heat capacity of rock matrix (J/kg/K)	790
Thermal conductivity of rock matrix (W/m/K)	2.5
Density of water (kg/m^3)	887.2
Dynamic viscosity of water (Pa·s)	1.42×10^{-4}
Compressibility of water (Pa^{-1})	5×10^{-10}
Specific heat capacity of water (J/kg/K)	4460
Longitudinal dispersivity (m)	0.2
Transverse dispersivity (m)	0.02
Partition coefficient (mm)	0.3

319
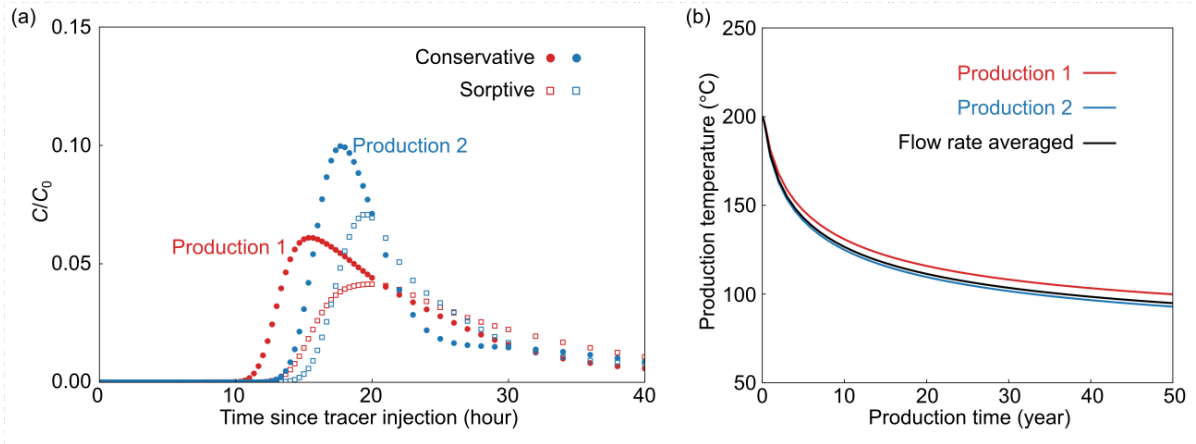
320
321   Fig. 3 Tracer and thermal modeling results for the synthetic field-scale EGS model. (a) Tracer
322   breakthrough curves at the two production wells. The monitored tracer concentration is
323   normalized by injection concentration C_0. (b) Thermal breakthrough curves at the two production
324   wells. The black curve is flow rate-averaged production temperature.

3.3 Dimensionality reduction of the aperture field

326   In real-world applications, fracture aperture distributions are not known *a priori*. To
327   represent inevitable biases in aperture distribution characterization, we intentionally assume a

328   log-normal aperture distribution for subsequent ES-MDA in this case study. Note that the
329   "ground truth" aperture field in Fig. 2 does not follow a log-normal distribution.

330   We use sequential gaussian simulations to generate N_r = 5,000 spatially correlated
331   aperture fields from a spherical variogram with a mean of 1 mm, a standard deviation of 0.83
332   mm and a correlation length of 100 m. All of the generated aperture fields follow a log-normal
333   distribution. Note that we ignore the anisotropy of the aperture field as seen in Fig. 2, another
334   deliberate erroneous bias introduced to test the robustness of the method. We then perform PCA
335   on these 5,000 sample aperture fields according to the procedures in Section 2.1 to obtain the
336   principal components. The level of details retained (i.e. fidelity) by aperture fields reconstructed
337   from equations (3) and (4) depends on the dimension of the latent space. If the hyper parameter l
338   = 5,000, the original aperture field can be fully reconstructed. With decreasing l, the
339   reconstructed aperture fields appear smoother (Fig. 4). Some fine features are missed in the
340   reconstructed aperture fields, but the major patterns are preserved.

341   In the following ES-MDA process, we select the first 200 principal components (l = 200)
342   as the basis for new aperture field generation. The goal of ES-MDA is therefore to invert for the
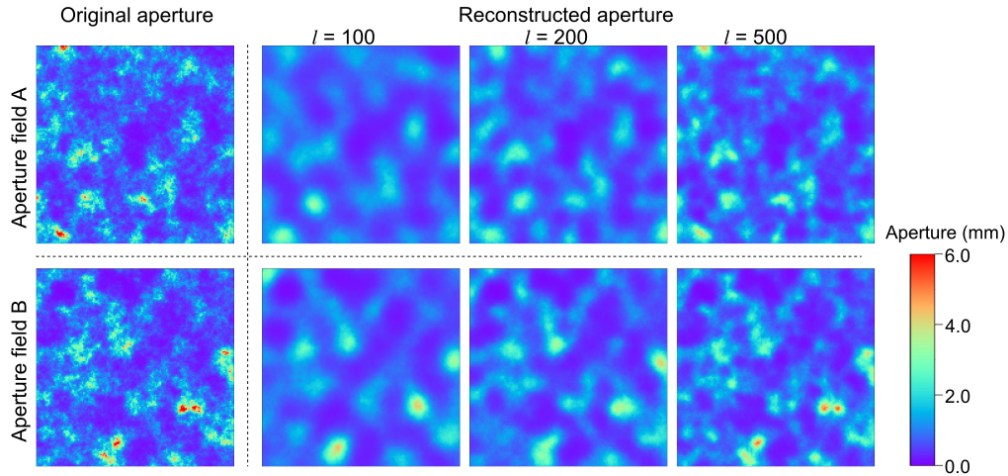343   200 latent parameters.

344
345   Fig. 4 Reconstruction of two aperture fields with varying numbers of principal components.
346   Approximately 61%, 76% and 86% of the total variance or "energy" in the original aperture
347   fields are preserved with l = 100, 200 and 500 respectively.

348   ### 3.4 ES-MDA on tracer, pressure and flow rate data

349   In this section, we use the ES-MDA as laid out in Section 2.2 to assimilate the tracer,
350   pressure and flow rate data in Section 3.2. Each tracer breakthrough curve in Fig. 3(a) contains
351   105 data points. Together with the pressure difference and the two flow rates, we have 423 data
352   points in total (N_d = 423). We add random gaussian noise to the data, using standard deviations
353   as follows: 1) For the tracer data, the standard deviation is 3% of the peak magnitude in Fig. 3(a).
354   2) For the pressure and flow rate data, the standard deviation is 1.5% of the observed values.
355   These standard deviations are used to calculate the covariance matrix of the measurement errors
356   $\mathbf{C_Y}$ in equation (6). The total data assimilation number is 12 (N_a = 12). We set gradually
357   decreasing inflation coefficients as suggested by Emerick and Reynolds (2013). After each
358   iteration, we decrease the inflation coefficient by 10%. According to equation (7), the inflation

359   coefficients for the 12 iterations are 22.9, 20.6, 18.5, 16.7, 15.0, 13.5, 12.2, 10.9, 9.8, 8.8, 7.9,
360   and 7.1 respectively.

361   We first generate 800 latent parameter sets as the prior ensemble (N_e = 800) by randomly
362   sampling from the standard normal distribution. For each latent parameter set in the prior
363   ensemble, we generate a prior aperture field using the PCA results in Section 3.3 and perform
364   tracer modeling to obtain the prior simulations of tracer, pressure and flow rate (Fig. 5).
365   Afterward, we use equation (6) to update the latent parameter sets for 12 iterations. In each
366   iteration, we repeat the aperture field generation and tracer modeling steps using the updated
367   latent parameter sets. After the last iteration, we obtain posterior latent parameter sets and
368   aperture fields. The tracer breakthrough curves simulated by the posterior aperture fields match
369   the "true" tracer breakthrough curves much better than those predicted by the prior aperture
370   fields (Fig. 5(a)). With the update of the latent parameter sets, the simulated pressure and flow
371   rate also gradually approach to the "true" values (Fig. 5(b)). The differences in posterior
372   simulations among the 800 realizations represent uncertainties from measurement errors
373   (Gaussian noise in this case) and biases in the prior knowledge of the aperture fields.
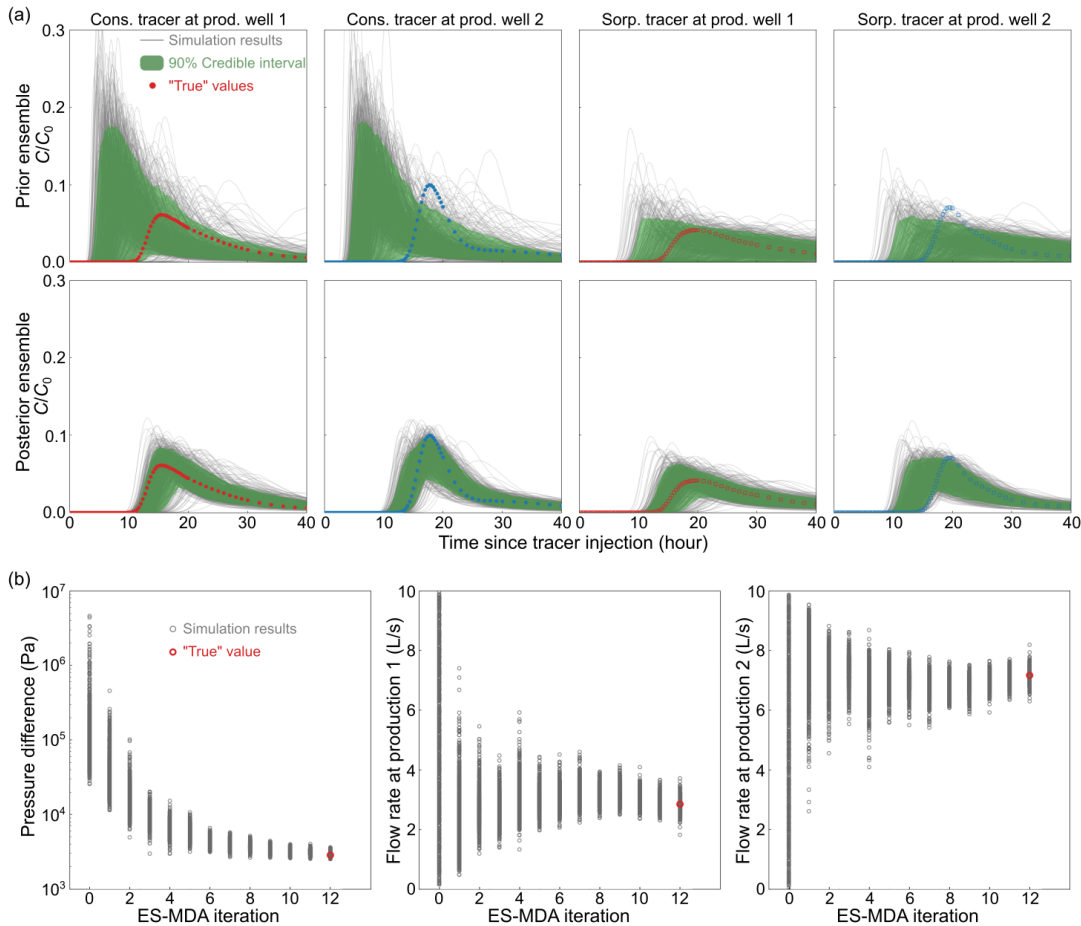

374

375   Fig. 5 Simulations of tracer, pressure and flow rate from prior and posterior realizations for the
376   synthetic field-scale model. (a) Comparison between the predicted and "true" tracer
377   breakthrough curves. The upper row shows the comparison for the prior ensemble, and the lower
378   row is the comparison for the posterior ensemble. All the predicted tracer breakthrough curves

379   from the 800 realizations in the ensemble are shown (grey curves). The green shadings are the
380   90% credible intervals for the predicted tracer breakthrough curves. (b) The evolution of the
381   predicted pressure and flow rate with respect to ES-MDA iterations. For each iteration, the
382   predicted pressure and flow rate from the 800 realizations are shown (grey circles). The "true"
383   values are annotated by red circles situated along the final iteration.

384   3.5 Analysis of aperture distribution and fracture flow characteristics

385   With the posterior ensemble from ES-MDA, we can analyze the spatial distribution of
386   aperture as well as flow characteristics in the fracture to compare with the synthetic "ground
387   truth". We first randomly select an aperture realization from the prior ensemble to compare with
388   the true aperture field. The true flow field (first row in Fig. 6) has two major flow channels
389   connecting the injection well and the two production wells respectively. However, the flow field
390   from the randomly selected prior realization (second row in Fig. 6) exhibits distinct flow patterns
391   with three flow channels connecting the injection and production wells. After 12 ES-MDA
392   iterations, the corresponding posterior realization's flow field (third row in Fig. 6) qualitatively
393   resembles the true flow field. The two major flow channels in the true flow field are
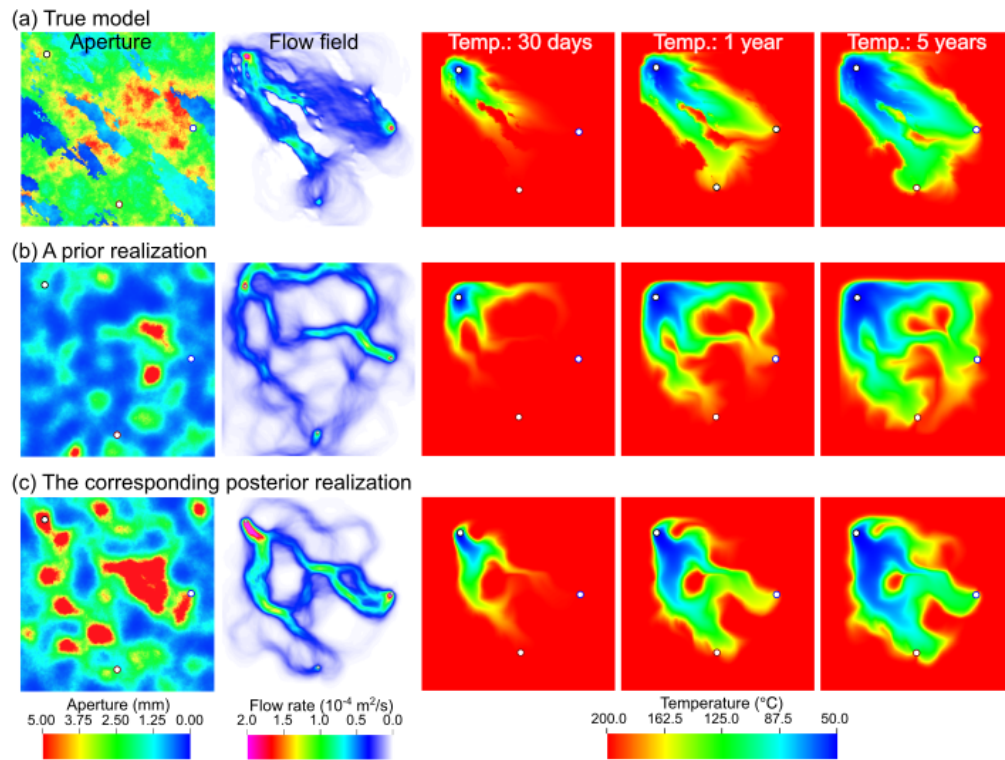394   approximately resolved.

395

Fig. 6 Comparison of aperture distribution, flow field and temperature (Temp.) evolution in the
fracture among (a) the true model, (b) a prior realization randomly selected from the prior
ensemble, and (c) the corresponding posterior realization from the posterior ensemble. The flow
rate is the volume of water passing a unit-length cross section of the fracture per unit time. Note
that we only show the temperature distribution on the fracture plane for clarity.

401   The average aperture from all 800 realizations is shown in Fig. 7. For the prior ensemble,
402   since each aperture realization is an independently generated random field, the average aperture

403   is almost uniform. The corresponding average flow field exhibits a relatively homogeneous
404   pattern among the injection and production wells without any remarkable flow channel. The
405   posterior aperture distributions, on the contrary, show significant common patterns among the
406   800 realizations. The average aperture for the posterior ensemble is far more heterogeneous than
407   that for the prior ensemble. Correspondingly, the average flow field for the posterior ensemble
408   exhibits strong flow channels between the injection and production wells, which are similar to
409   that in the true flow field in Fig. 6.

410   It is important to note that the posterior ensemble's average aperture field is still quite
411   different from the "ground truth" aperture in Fig. 2. This is not surprising because the true
412   aperture field follows a complex distribution that is not covered by the constructed parameter
413   space for the ensemble. Matching the aperture field is not a goal of our approach. The success of
414   the method is measured by its ability to predict the thermal performance as presented in the next
415   sub-section. As thermal response of the system is directly determined by the flow distribution but
416   only indirectly affected by the aperture distribution, the predicted thermal response could be
417   accurate as long as the flow field is reasonably resolved, even if the underlying aperture field is
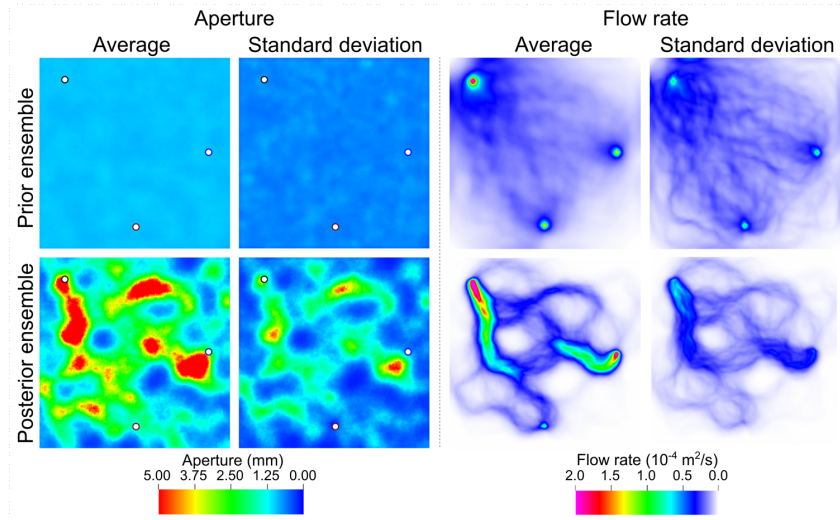418   very different from the ground truth.

419

420   Fig. 7 Average and standard deviation of aperture distribution and flow rate calculated from prior
421   (upper row) and posterior (lower row) ensembles.

422   3.6 Thermal performance prediction

423   To investigate the suitability of the posterior ensemble for predicting thermal
424   performance, we perform thermal simulations on both the prior and posterior ensembles. Fig. 8
425   shows the predicted flow rate-averaged thermal breakthrough curves from these realizations.
426   Results for only 50 randomly selected realizations are shown to avoid over-crowding the
427   visualization. Most of the prior realizations have a slower temperature decrease compared with
428   the true temperature response, and there is a large uncertainty among the predictions from the 50
429   prior realizations (Fig. 8(a)). This is expected because the prior ensemble was essentially non-
430   calibrated. On the other hand, the predictions from the posterior realizations show a much
431   smaller uncertainty, and the true temperature response is reasonably predicted (Fig. 8(b)). By
432   conditioning the aperture field on tracer, pressure and flow rate data through the proposed
433   framework, we successfully resolve the major flow channels in the true flow field and the

434 obtained posterior aperture distributions are capable of predicting long-term thermal
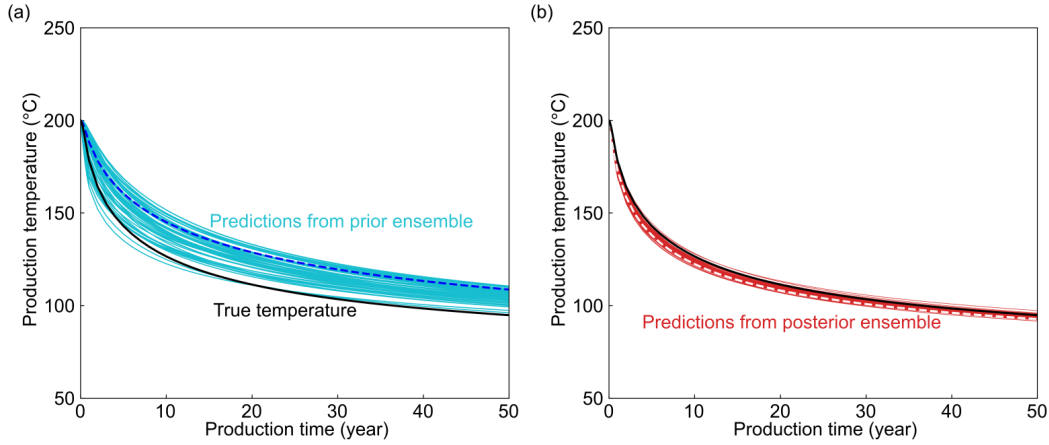435 performance.

436

437 Fig. 8 Prediction of thermal performance (flow rate-averaged thermal breakthrough curve) from
438 the prior (a) and posterior (b) ensembles. The solid black line is the "true" thermal breakthrough
439 curve. The dash blue line (left) and dash white line (right) are the results for the realization
440 visualized in Fig. 6. The cyan (left) and red (right) lines are the results for 50 randomly selected
441 aperture realizations from the prior and posterior ensembles, respectively.

442   The thermal breakthrough curves corresponding to the prior and posterior realizations in
443 Fig. 6 are also shown in Fig. 8 (dash lines). To understand the greatly improved thermal
444 predictive ability of the posterior realization, the third to fifth columns in Fig. 6 further compare
445 the simulated temperature evolutions in the fracture corresponding to the true aperture field as
446 well as the prior and posterior aperture fields. The temperature distribution in the fracture highly
447 depends on the underlying flow patterns. Because the posterior aperture reasonably resolves the
448 true flow field, the temperature evolution predicted by the posterior aperture is quite accurate.

449   3.7 Effect of incorporating different data types in data assimilation

450   In the above analysis, we incorporate all the available data, including conservative and
451 sorptive tracer data, pressure data and flow rate data, in ES-MDA for aperture inference. This
452 section investigates the effects of incorporating different data types by separately assimilating
453 these data with ES-MDA. Four extra ES-MDAs are performed: 1) Conservative tracer data only,
454 2) conservative tracer data as well as pressure and flow rate data, 3) Sorptive tracer data only,
455 and 4) both conservative and sorptive tracer data, without pressure or flow rates. For each ES-
456 MDA, we use the same procedure as that in Section 3.4 to generate a posterior ensemble, and
457 perform thermal simulations to predict thermal performance (Fig. 9). Compared with the prior
458 predictions in Fig. 8(a), all the posterior predictions in Fig. 9 show a reduced uncertainty. When
459 only conservative tracer data are assimilated, the predicted temperature is systematically higher
460 than the true temperature, indicating systematic biases in the obtained posterior aperture
461 distributions. Note that the prior ensemble has the same bias, namely higher predicted
462 temperature. The bias in the posterior predictions is likely due to the conservative tracer recovery
463 being insensitive to this bias, instead of being introduced by the conservative tracer data itself.
464 Adding pressure and flow rate data to ES-MDA somewhat improves the prediction accuracy, but
465 the results are still poor. Compared with conservative tracer data, sorptive tracer data is more

466 effective in constraining the prediction of temperature response as demonstrated by the
467 significantly better results in Fig. 9(c) than (a). This is because sorptive tracer data is more
468 sensitive to the interaction area between fracture fluid and surrounding rock formations than
469 conservative tracer, and therefore can better characterize fluid-rock interaction area which is
470 critical for thermal prediction. When conservative and sorptive tracer data are assimilated
471 simultaneously, the temperature response can be accurately predicted. Tracer data, especially
472 sorptive tracer data, are critical for the proposed framework to correctly characterize fracture
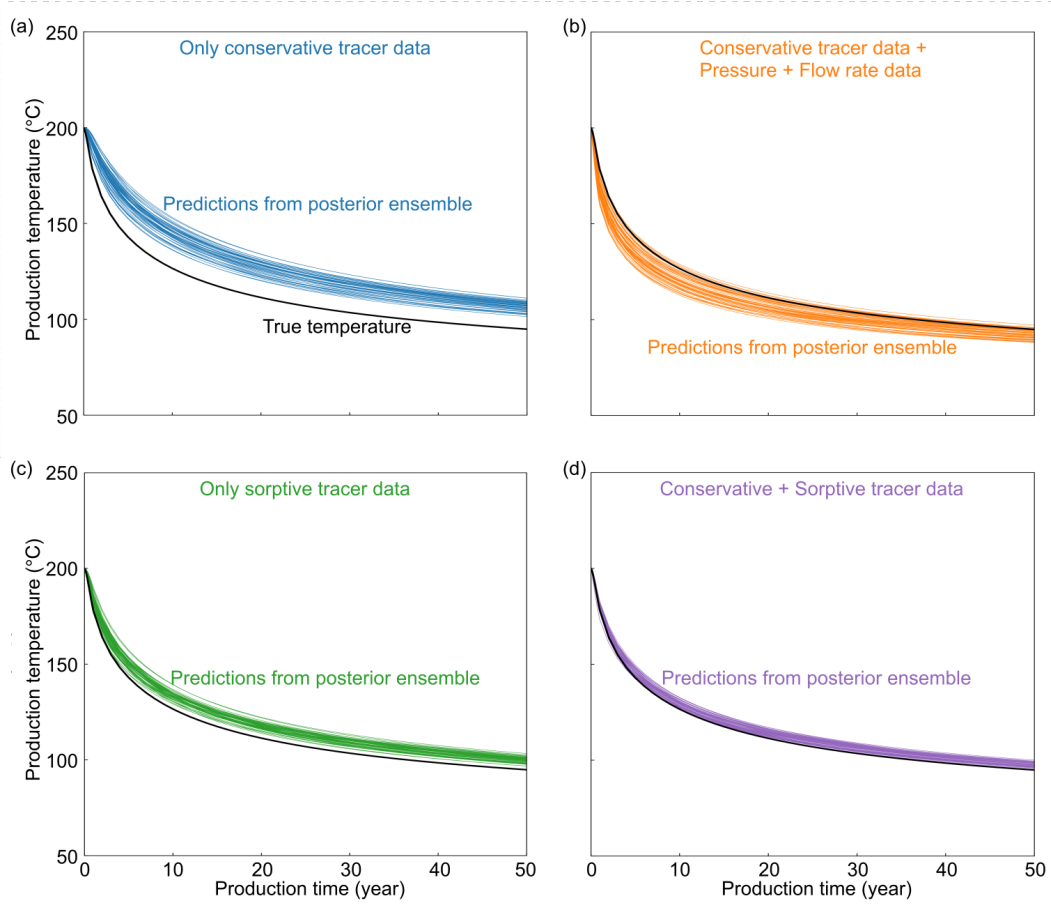473 flow and predict thermal performance.

474

Fig. 9 Prediction of thermal performance (flow rate-averaged thermal breakthrough curve) from
posterior ensembles obtained by assimilating different data types. The assimilated data type is
annotated in each plot: (a) Conservative tracer data. (b) Conservative tracer data, pressure and
flow rate data. (c) Sorptive tracer data. (d) Conservative and sorptive tracer data.

479 According to the predictions in Figs. 8 and 9, we can estimate the production life span of
480 the field scale EGS model. We use a temperature threshold of 120 °C to determine the "useable"
481 life of an EGS, i.e., the EGS terminates when the production temperature decreases to below
482 120 °C. Fig. 10 compares the estimated production life spans from the prior ensemble as well as
483 the five posterior ensembles obtained by assimilating different data types. The uncertainty of the
484 production life span (difference between minimum and maximum predictions) is approximately
485 22 years for the prior ensemble and decreases to less than 4 years for the two posterior ensembles
486 with both conservative and sorptive tracer data assimilated. It is also worth mentioning that the

487 mean production life span estimated from the two posterior ensembles is very close to the true
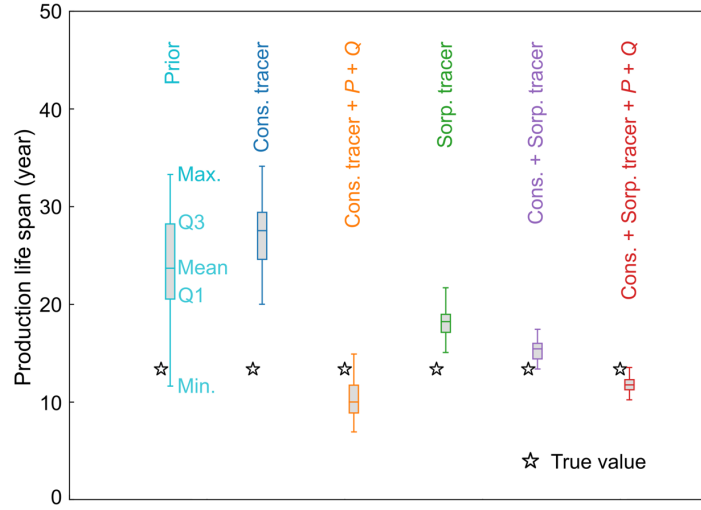488 value.

489

490 Fig. 10 Production life span estimated from temperature response predictions. The box plots
491 show the minimum, maximum, mean, as well as the 25% (Q1) and 75% (Q3) percentiles. *P* and
492 *Q* represent the pressure and flow rate data respectively.

4 Validation based on a meso-scale field experiment

494   In this section, we apply the proposed framework to a meso-scale field experiment to
495 further validate its capability in real-world applications. The meso-scale field experiment was
496 performed at the Altona Field Laboratory (AFL) located in the Altona Flat Rocks region in
497 northern New York State, USA (Hawkins et al., 2017a, 2018, 2021). The testbed of the field
498 experiment involves a sub-horizontal fracture approximately 7.6 m below the ground surface. A
499 series of tests were conducted in the testbed to investigate heat and mass transfer processes
500 relevant to geothermal applications, including conservative and sorptive tracer tests as well as a
501 thermal test (Hawkins et al., 2017a, 2018). The obtained tracer and thermal data provide a unique
502 opportunity to validate the proposed framework.

503   The well configuration and geological condition of the testbed has been reported in the
504 literature (Hawkins et al., 2017a, 2018, 2020) and therefore not repeated here. In what follows,
505 we first briefly describe relevant field measurements, and then use the proposed framework to
506 infer the aperture distribution in the sub-horizontal fracture and predict production temperature
507 during the thermal test.

508   4.1 Tracer and thermal data at the AFL testbed

509   Both the tracer and thermal tests were performed through an injection well and a
510 production well connected by the sub-horizontal fracture. The distance between the injection and
511 production wells was approximately 14.1 m. To perform tracer tests, water was continuously
512 circulated between the injection and production wells at a constant volumetric flow rate of 5.82
513 L/min. A salt of Cesium-Iodide (CsI) was used as a combined sorptive/conservative tracer, with
514 the cesium cation as a sorptive tracer and the iodine anion as a conservative tracer. The field

515   results of the multi-component tracer tests are shown in Fig. 11(a). The arrival times of peak
516   concentration are almost identical for the iodine and cesium ions, but the normalized peak
517   magnitude is smaller for cesium. As discussed in Hawkins et al. (2018), this apparent deviation
518   from an equilibrium model results from rate-limited adsorption. The second peaks at
519   approximately 40 min were mainly caused by the continuous reinjection of produced fluids
520   during the tracer tests (Hawkins et al., 2020). To determine the adsorption reaction parameters of
521   cesium ions, Hawkins et al. (2018) performed two batch reactor experiments in which cesium
522   ions dissolved in water were adsorbed onto two rock samples collected at roughly 17 m below
523   the testbed surface. The measured partition coefficients (P_f) are 7.8 and 16.6 cm, and the first-
524   order adsorption rates are 0.4 and 1.33 d^{-1}. In addition to the tracer tests, a pressure test
525   conducted in 2012 recorded a pressure loss of 433 Pa between the injection and production wells
526   under an injection volumetric flow rate of 4.2 L/min. In subsequent ES-MDA analysis, we
527   assume a linear relationship between injection rate and pressure loss, and therefore the pressure
528   loss during the tracer test with a volumetric flow rate of 5.82 L/min can be calculated as 600 Pa.

529   The thermal test was performed by continuously injecting heated water (74 °C) into the
530   fracture at a constant volumetric flow rate of 5.7 L/min for six days. The measured temperature
531   response at the production well indicated an extremely rapid thermal breakthrough (Fig. 11(b)).
532   After six days, the production well fluid temperature increased approximately 17.7 °C from the
533   initial value of 11.7 °C to a final value of 29.4 °C.
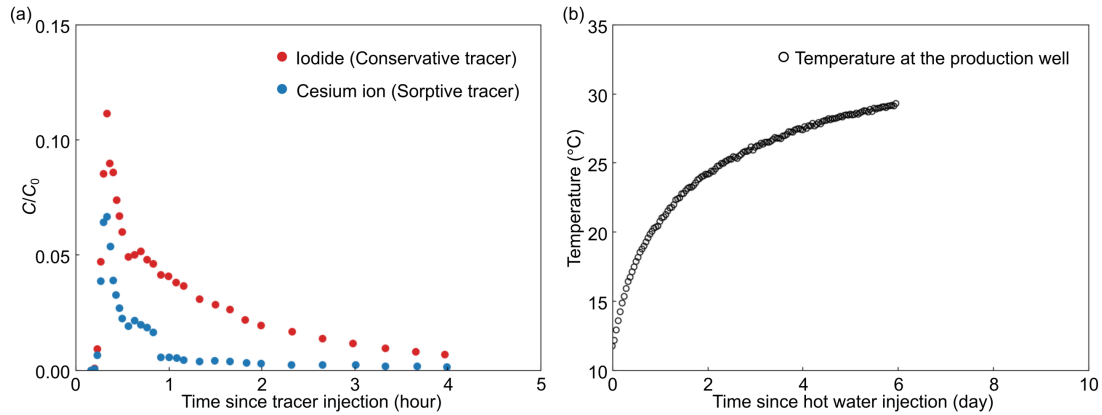

534
535   Fig. 11 Results of the tracer and thermal tests at the Altona Field Laboratory testbed. (a) Tracer
536   breakthrough curves at the production well for iodine and cesium ions. The monitored tracer
537   concentration is normalized by injection concentration C_0. (b) Thermal breakthrough curve at the
538   production well during the thermal test.

539   4.2 Numerical model for tracer and thermal simulation

540   We develop a $200 \times 200 \times 20$ m³ model to simulate the tracer and thermal processes in
541   the AFL testbed (Fig. 12). A 32×32 m² horizontal fracture is assumed 7.6 m below the top
542   surface of the model. The fracture is represented by a 4 mm layer with an in-plane mesh
543   resolution of 0.2 m × 0.2 m. The mesh resolution of the rock is 0.2 m × 0.2 m × 0.5 m near the
544   fracture and gradually increases to 10 m × 10 m × 2 m in the far field. The total element number
545   in the model is approximately 840,000. Based on prior knowledge from Ground Penetrating
546   Radar (GPR) surveys (Hawkins et al., 2018), we assume an oriented aperture distribution from
547   the injection well towards the production well (Fig. 12(b)). Similar to the field-scale EGS model

548   in Section 3, we generate 5,000 oriented 160 × 160 log-normal random fields and use PCA to
549   represent the aperture field with a 200-dimensional latent space. The first 200 principal
550   components can preserve approximately 62.7% of the total variance in original aperture fields.

551   For tracer modeling, we only consider the 2D fracture as the porosity and permeability of
552   the surrounding Potsdam Sandstone are negligible relative to the target fracture (Table 2). The
553   fracture boundaries are assumed impermeable. The reinjection of produced fluid is accounted for
554   by specifying tracer injection concentration according to the simulated tracer concentration at the
555   production well. We consider rate-limited adsorption process for the tracer modeling of cesium
556   ion, with the first-order adsorption rate and partition coefficient estimated from the
557   measurements mentioned in Section 4.2 (Table 2). Note that we use a relatively large partition
558   coefficient within the measured range (7.8 – 16.6 cm). For thermal modeling, we consider the
559   whole computational domain in Fig. 12. The upper, lower and lateral model boundaries are
560   assumed impermeable to both fluid and heat. Key parameters for tracer and thermal modeling are
561   obtained from the literature (Hawkins et al., 2017a, 2020), as summarized in Table 2.
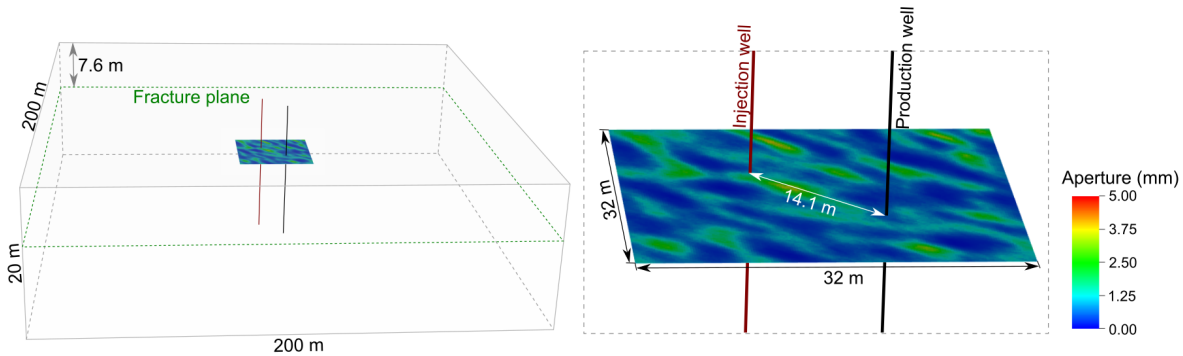

562

563   Fig. 12 Three-dimensional model for the Altona Field Laboratory testbed. Note that the scales in
564   the horizontal and vertical directions are different.

565

566   Table 2 Parameters for tracer and thermal modeling in the AFL testbed.

Parameter	Value
Porosity of rock	0.01
Permeability of rock (m^2)	1×10^{-16}
Density of rock (kg/m^3)	2500
Specific heat capacity of rock (J/kg/K)	1000
Thermal conductivity of rock (W/m/K)	7.6
Initial temperature in the testbed (°C)	11.7
Density of water (kg/m^3)	1000
Dynamic viscosity of water (Pa·s)	0.001
Compressibility of water (Pa^{-1})	5×10^{-10}
Specific heat capacity of water (J/kg/K)	4200

Longitudinal dispersivity (m)	0.1
Transverse dispersivity (m)	0.01
First-order adsorption rate of cesium ion (d^{-1})	0.865
Partition coefficient of cesium ion (cm)	15.0

567   4.3 Numerical model for tracer and thermal simulation

568   The conservative tracer, sorptive tracer and pressure loss data are assimilated
569   simultaneously using ES-MDA. The total number of data points is 66 ($N_d = 66$). The standard
570   deviations are assumed to be 0.003, 0.0024 and 6.5 Pa for the conservative tracer, sorptive tracer
571   and pressure data respectively. The total data assimilation number is 15 ($N_a = 15$), and the
572   ensemble size is 432 ($N_e = 432$).

573   The measured tracer breakthrough curves for iodine and cesium ions are appropriately
574   reproduced with the obtained posterior ensemble as shown in Fig. 13(a). The pressure loss
575   between the injection and production wells simulated by the posterior ensemble is also consistent
576   with the field measurements (Fig. 13(b)).
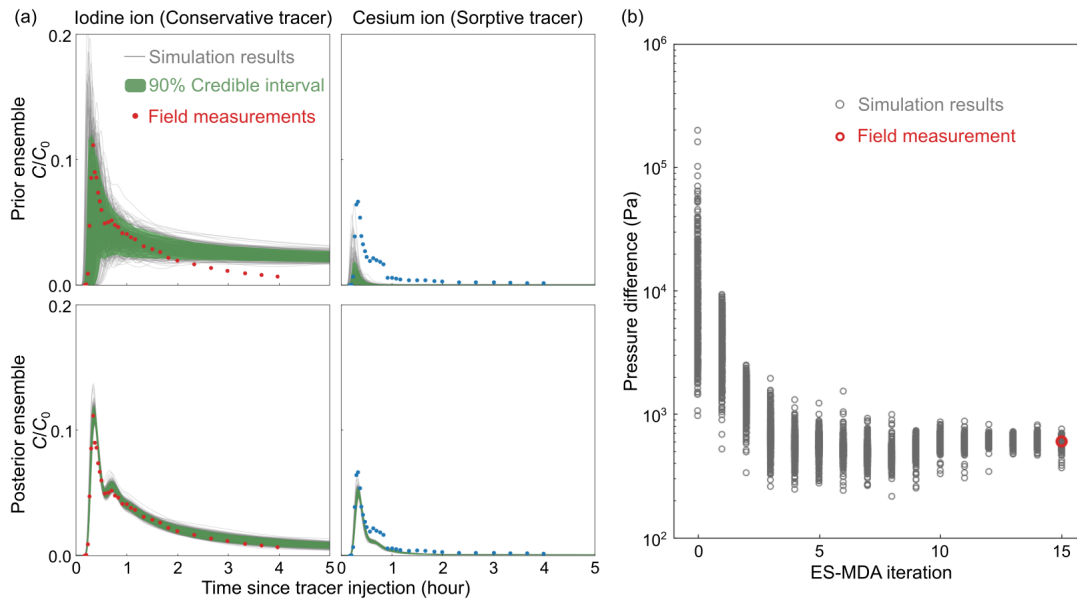

577

578   Fig. 13 Simulation results of tracer breakthrough curve and pressure loss at the AFL testbed. (a)
579   Comparison between the simulated (grey curves) and true tracer breakthrough curves (dots) from
580   prior and posterior ensembles. (b) Change of the simulated pressure loss with ES-MDA
581   iterations. Simulation results are shown by grey circles, and the true value is annotated by the red
582   circle.

583   4.4 Analysis of aperture distribution and fracture flow characteristics

584   Fig. 14 compares the aperture distribution and flow field calculated from prior and
585   posterior ensembles. Similar to the results of the previous field scale EGS model, the average
586   fracture aperture distribution obtained from prior ensemble is quite uniform, and no remarkable
587   flow channel is observed in the average flow field (Fig. 14(a)). After ES-MDA updates, the average

588   aperture and flow field from posterior ensemble reveal a narrow flow channel connecting the
589   injection and production wells (Fig. 14(b)). This striking feature is essential for the fit of the tracer
590   breakthrough curve of the sorptive cesium ion. For prior realizations, since the flow field between
591   the injection and production wells is relatively uniform, the effective interaction area (i.e., the
592   fracture-fluid interfacial surface area or "flow-wetted" surface area) between fluid and surrounding
593   rocks is relatively large. As a result, a large portion of the injected cesium ions are adsorbed by the
594   rock and the simulated tracer concentrations at the production well are smaller than the
595   measurements (Fig. 13(a)). For posterior realizations, since most of the fluid is constrained in the
596   narrow flow channel, the fluid-rock interaction area is dramatically reduced, and therefore the
597   simulated tracer breakthrough curves of cesium ion can appropriately match the measurements.
598   Such a narrow flow channel is also consistent with previous GPR surveys (Hawkins et al., 2018).
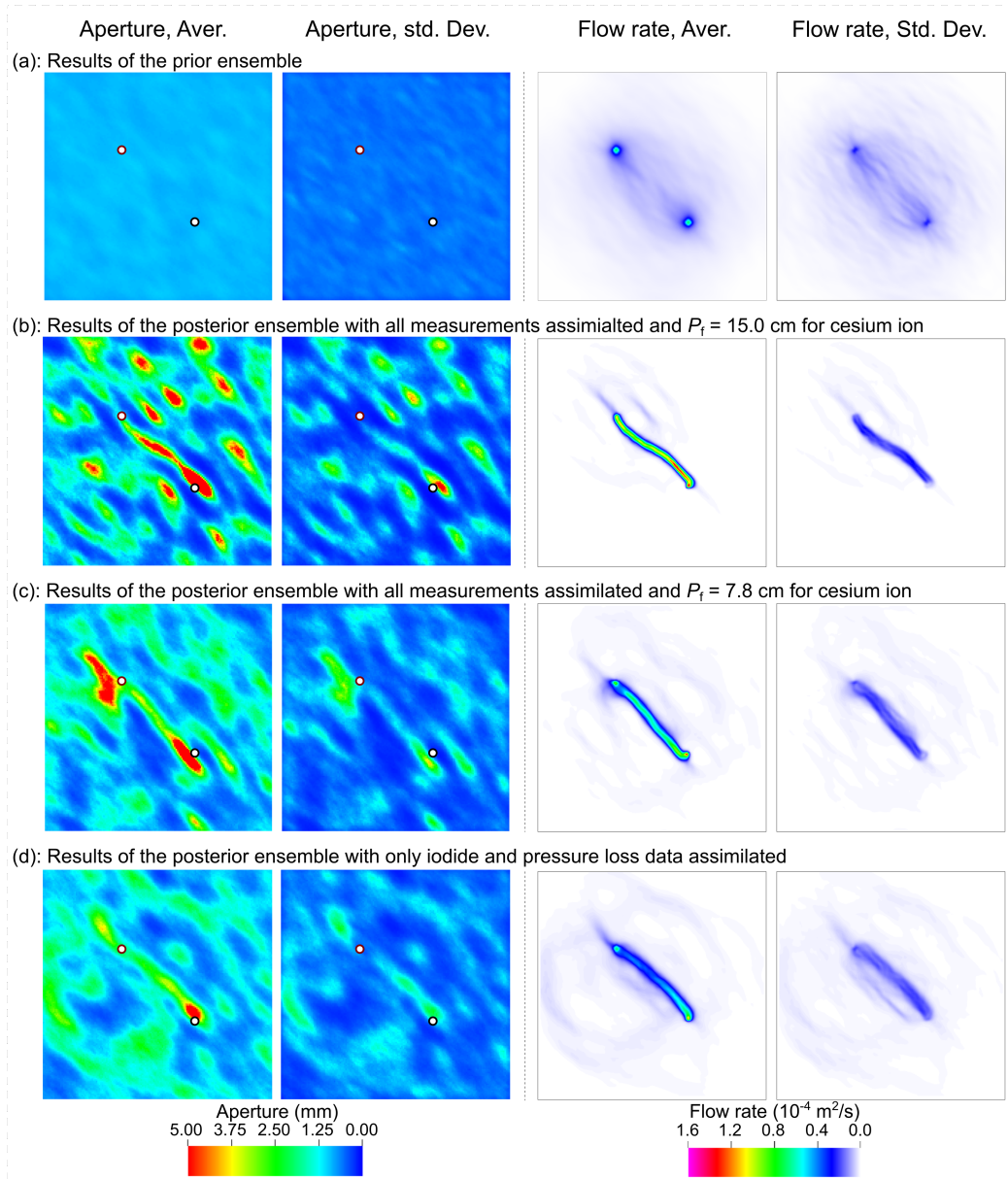

599

600   Fig. 14 Average (Aver.) and standard deviation (Std. Dev.) of aperture distribution and flow rate
601   calculated from prior and posterior ensembles. (a) Results for the prior ensemble. (b) Results for

602   the posterior ensemble of the baseline ESMDA which assimilates all measurements
603   simultaneously and uses a relatively large partition coefficient (15.0 cm) for cesium ions. (c)
604   Results for the posterior ensemble of the ESMDA which assimilates all measurements
605   simultaneously and uses a relatively small partition coefficient (7.8 cm) for cesium ions. (d)
606   Results for the posterior ensemble of the ESMDA which only assimilates iodine tracer and
607   pressure loss data.

608   We use a relatively large partition coefficient (15.0 cm) for cesium ions in the above ES-
609   MDA. However, as mentioned previously, the measured partition coefficients from two batch
610   reactor experiments are 7.8 and 16.6 cm, indicating that there exists uncertainty in the
611   appropriate value of the partition coefficient. To examine the impact of an uncertain partition
612   coefficient, we perform a second ES-MDA using a relatively small partition coefficient (7.8 cm)
613   for cesium ions. The obtained posterior ensemble can also match the tracer and pressure
614   measurements, and Fig. 14(c) shows the corresponding average aperture distribution and flow
615   rate in the fracture. The flow field is more diffuse than that in Fig. 14(b). Besides a major flow
616   channel similar to that in Fig. 14(b), several minor flow channels connecting the injection and
617   production wells appear. These minor flow channels enlarge the interaction area between fluid
618   and rock so that the tracer measurements of cesium ion can be matched with a relatively small
619   partition coefficient. We also perform a third ES-MDA that only assimilates the iodine tracer and
620   pressure loss data. The calculated average flow field shows a further scattered flow pattern
621   between the injection and production wells (Fig. 14(d)). The comparison in Fig. 14 indicates that
622   the partition coefficient has significant impacts on fracture flow characterization.

623   4.5 Analysis of temperature response at the production well

624   With the obtained prior and posterior ensembles, we now simulate the water injection test
625   and predict the temperature response at the production well. For each ensemble in Fig. 14, we
626   randomly select 30 realizations to perform thermal modeling. The predicted temperature rise from
627   the prior ensemble is much lower than the measured production temperature, and the results from
628   different realizations show a significant uncertainty (Fig. 15(a)). This is because randomly
629   generated aperture distributions in the prior ensemble result in diffuse flow patterns between the
630   injection and production wells (Fig. 14(a)). Fluid-rock interaction area is relatively large, retarding
631   the temperature increase at the production well. The predicted temperature increase at the end of
632   the hot water injection test varies between 0.0 to 6.0 °C among the 30 realizations (Fig. 15(a)),
633   which are much smaller than the measured temperature increase (17.7 °C) in the field.

634   For the posterior ensemble in Fig. 14(b), the interaction area between fluid and rocks is
635   largely constrained within the narrow flow channel, and therefore the predicted temperature at the
636   production well increases rapidly and agrees well with the measurements (Fig. 15(b)). The
637   predicted temperature increase after six days hot water injection (17.3 to 19.8 °C) is close to the
638   measured temperature increase. For the posterior ensemble in Fig. 14(c), the fluid-rock interaction
639   area is larger than that in Fig. 14(b) because of the minor flow channels. Therefore, the predicted
640   production temperature is smaller than that predicted by the posterior ensemble in Fig. 14(b), and
641   cannot match the measured production temperature (Fig. 15(c)). For the posterior ensemble in Fig.
642   14(d), the fluid-rock interaction area is further enlarged, and the corresponding temperature
643   increase at the production is further reduced (Fig. 15(d)). However, it is worth mentioning that
644   although the temperature predictions in Fig. 15(c) and (d) fail to match the field measurements,
645   they are still better than the predictions from the prior ensemble. Conservative tracer data and

646 pressure data provide useful information for aperture inference and thermal prediction, but sorptive
647 tracer data is indispensable to correctly predict temperature response. Hawkins et al. (2020) also
648 analyzed the tracer and thermal tests in the AFL testbed. They employed a genetic algorithm (GA)
649 to infer the aperture distribution using a conservative tracer (C-Dot) and pressure data, and then
650 predicted the production temperature. Their results also revealed a narrow flow channel of roughly
651 1.5 m width between the injection and production wells, but the predicted production temperatures
652 were smaller than field measurements. Incorporating sorptive tracer data in GA might be able to
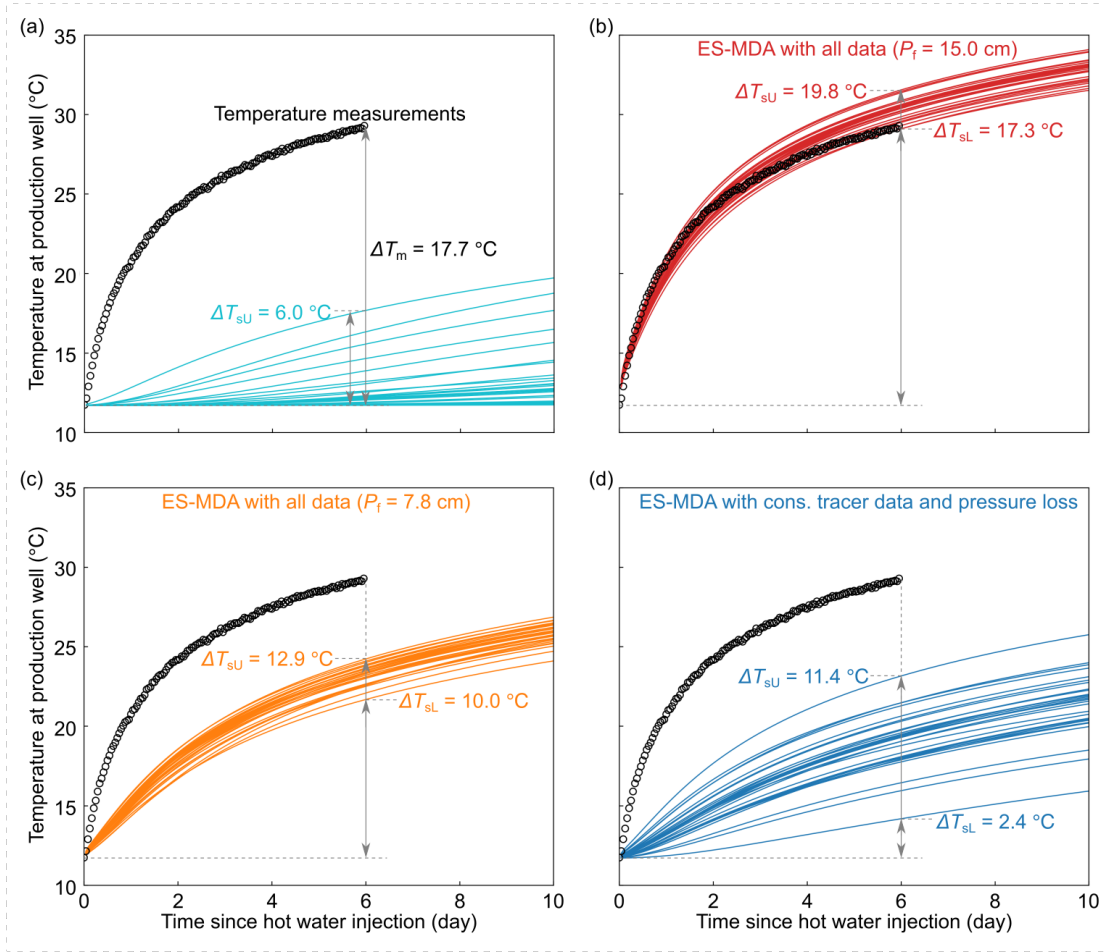653 improve the prediction of production temperature.

654

655 Fig. 15 Predicted and measured temperature responses at the production well during the hot
656 water injection test at the AFL testbed. Temperature increases at the end of the test are annotated.
657 ΔT_{m} denotes the measured temperate increase, and ΔT_{sU} and ΔT_{sL} are upper and lower bounds of
658 the predicted temperature increase. Results predicted by different ensembles are shown: (a) Prior
659 ensemble. (b) ~ (d) Posterior ensembles obtained by assimilating different data and using
660 different partition coefficients (P_{f}). The four sub-figures are corresponding to the four rows in
661 Fig. 14.

662 **5 Discussions**

663   5.1 Gaussian and non-Gaussian parameter fields

664   An important premise of the proposed framework is that model parameters follow a
665 Gaussian or log-normal distribution. On the one hand, PCA is only applicable to random fields
666 that can be fully characterized by two-point statistics (Liu and Durlofsky, 2020), such as the
667 Gaussian fields used in the present study. On the other hand, ES-MDA requires a Gaussian
668 parameter distribution, otherwise its performance could be severely degraded (Canchumuni et
669 al., 2020; Zhang et al., 2020). As mentioned in Section 2.1, latent parameters from PCA follow
670 the standard normal distribution, which perfectly meet the Gaussian requirement of ES-MDA.

671   Although a Gaussian parameter field (aperture or permeability) is a reasonable
672 assumption for many subsurface reservoirs, a non-Gaussian parameter field, such as a
673 binary/ternary facies field, has been widely adopted to account for highly channelized reservoirs
674 (Lochbühler et al., 2014; Hakim-Elahi and Jafarpour, 2017; Tang et al., 2020). Directly applying
675 the proposed framework to invert for such multi-facies fields inevitably leads to inaccurate
676 inversion results since the proposed framework always assumes a Gaussian (or log-normal)
677 parameter field to enable the use of PCA for dimensionality reduction.

678   However, an important finding from the present study is that a Gaussian field is able to
679 reproduce highly channelized flow patterns from a non-Gaussian field, and thus provide accurate
680 predictions of reservoir performance. Although the inferred aperture/permeability field might be
681 inaccurate, the underlying flow patterns can be appropriately resolved by matching tracer
682 measurements. For the example in Fig. 2, the "true" aperture field is highly channelized and does
683 not follow a Gaussian or log-normal distribution. It is not even within the Gaussian parameter
684 space that we construct for subsequent ES-MDA. Nevertheless, the flow fields simulated based
685 on the inferred Gaussian aperture fields closely resemble the true flow field (Fig. 7). This is not
686 surprising because tracer recovery is more directly affected by the flow field than by the aperture
687 field. As a result, the thermal performance is accurately predicted (Figs. 6 and 8).

688   Another solution to address the issue of non-Gaussian parameter field is developing
689 effective parameterization methods that can map high-dimensional non-Gaussian fields to low-
690 dimensional latent parameters that follow Gaussian distributions. In fact, the parameterization of
691 complex geological structures such as binary/ternary facies fields is currently an active research
692 area. Various methods have been proposed, including optimization-based PCA (O-PCA) (Vo and
693 Durlofsky, 2014), discrete cosine transform (Jafarpour and McLaughlin, 2007), and deep
694 learning algorithms such as CNN-PCA (Liu and Durlofsky, 2020), variational autoencoder
695 (VAE) (Laloy et al., 2017; Canchumuni et al., 2019; Mo et al., 2020), and generative adversarial
696 network (GAN) (Laloy et al., 2018; Canchumuni et al., 2020). These parameterization methods
697 have been successfully used for the inference of non-Gaussian permeability fields through
698 ensemble-based data assimilation methods (Canchumuni et al., 2019, 2020; Bao et al., 2020).

699   5.2 Discrete fracture network (DFN)

700   Both the synthetic and field cases in the present study have a predominant fracture in the
701 reservoir. However, for many naturally fractured reservoirs, fluid flow may involve multiple
702 interconnected fractures that form a discrete fracture network (DFN). For such reservoirs, the
703 fracture flow patterns depend not only on the aperture distributions of individual fractures but
704 also the geometry of DFN. Extending the proposed framework from a single fracture to DFNs

705 requires an effective parameterization method that can represent salient information in DFNs
706 relevant to fluid flow with appropriately compromised model complexities.

707   Current approaches for DFN parameterization usually represent each single fracture by
708 parameters describing its location, orientation, size and aperture to allow individual tuning of
709 fractures (Dorn et al., 2013; Somogyvári et al., 2017; Ma et al., 2020). Such a parameterization
710 induces an extremely high-dimensional parameter space. Moreover, since the number of
711 fractures is not known *a priori*, the dimensionality may vary in the inversion process, making
712 most inversion/data assimilation methods inapplicable, including the proposed framework. A
713 possible solution to this difficulty is using advanced deep learning algorithms (such as VAE and
714 GAN) to generate high-fidelity DFN models from low-dimensional latent spaces. The capability
715 of GAN and VAE in reproducing complex data structures and preserving data statistics has been
716 widely reported. Their application in parameterizing DFNs with highly discontinuous structures
717 deserves further investigations.

718   5.3 Implications for subsurface characterization and analysis

719   Although tracer testing has been widely used for subsurface characterization, how to
720 effectively interpret tracer data and whether the interpretation results (permeability or aperture
721 distribution) can correctly predict long-term performance has not been adequately elucidated
722 previously. The present study attempts to answer these questions and provides a new framework
723 for the characterization and analysis of fractured reservoirs. The analyses of a synthetic EGS
724 model and a field geothermal test indicate that tracer data contain essential information regarding
725 subsurface flow characteristics. The proposed framework is able to retrieve necessary flow
726 information to accurately predict thermal performance in the two examples considered here.
727 Moreover, because the framework uses an ensemble-based data assimilation method,
728 uncertainties arising from biased prior knowledge and measurement errors can be naturally
729 tackled. We demonstrate how these uncertainties propagate to the inverted aperture distribution
730 and fracture flow pattern, and further to the thermal prediction in the two cases.

731   An important implication for real-world applications is that both conservative and
732 sorptive tracer tests need to be conducted to sufficiently characterize subsurface fractures for
733 thermal prediction. Both the synthetic and field cases in the present study indicate that
734 conservative tracers alone are unable to constrain fracture aperture, leading to biased predictions
735 with large uncertainties. In several previous attempts to predict thermal performance from tracer
736 data (Vogt et al., 2012b; Hawkins et al., 2020; Wu et al., 2021), the predicted thermal
737 performance either indicates significant uncertainty or cannot qualitatively match field
738 measurements. A possible reason is that only conservative tracer data was used for
739 aperture/permeability inversion in these attempts. In addition, when sorptive tracer data is
740 available, the sorption parameters such as partition coefficient need to be carefully measured.
741 The field case clearly shows the remarkable impact of partition coefficient on aperture inversion
742 and thermal prediction (Figs. 14 and 15).

743 **7 Conclusions**

744   We proposed a tracer data interpretation framework to predict the long-term thermal
745 performance of EGS from tracer tests. The framework first inverts for the spatial distribution of
746 fracture aperture through an ensemble-based data assimilation method, and then uses the
747 inversion results to predict thermal performance. A synthetic case with a field-scale EGS model

748 and a real-world case involving meso-scale tracers and thermal tests were analyzed to
749 demonstrate the capability of the framework. For both cases, thermal performance was
750 accurately predicted and the associated uncertainty was appropriately quantified through the
751 obtained posterior model ensembles. By interpreting practically available tracer, pressure and
752 flow data, the framework can provide informative guidance for reservoir optimization and long-
753 term risk management.

754   The correct prediction of thermal performance requires the joint assimilation of
755 conservative and sorptive tracer data. Sorptive tracer data is indispensable to properly
756 characterize fracture flow patterns, especially the effective fluid-rock interaction area which is
757 critical for thermal prediction. Analysis without of sorptive tracer data tends to overestimate
758 fluid-rock interaction, leading to biased prediction of thermal performance with relatively large
759 uncertainties.

760   Besides tracer, pressure and flow data, other types of data such as deformation and
761 seismic data can also be interpreted using the proposed framework. Since physical models for
762 deformation and seismic modeling are different from that for tracer transport, we need to replace
763 the forward simulation in the framework accordingly. Of course, the predictive ability of the
764 interpretation results highly depends on the relationship between the data being interpreted and
765 the quantity to be predicted. For the EGS examples in the present study, the strong connection
766 between tracer transport and heat extraction processes is the basis for predicting thermal
767 performance from tracer data.

768 Acknowledgments, Samples, and Data

778 References

779 Ayling, B. F., Hogarth, R. A., Rose, P. E. (2016). Tracer testing at the Habanero EGS site,
780   central Australia. *Geothermics*, *63*, 15-26.
781 Bao, J., Li, L., Redoloza, F. (2020). Coupling ensemble smoother and deep learning with
782   generative adversarial networks to deal with non-Gaussianity in flow and transport data
783   assimilation. *Journal of Hydrology*, *590*, 125443.
784 Berkowitz, B. (2002). Characterizing flow and transport in fractured geological media: A review.
785   *Advances in Water Resources*, *25*, 861-884.
786 Brown, D. W., Duchane, D. V., Heiken, G., Hriscu, V. T. (2012). Mining the Earth's Heat: Hot
787   Dry Rock Geothermal Energy. Springer, Berlin.
788 Canchumuni, S. W. A., Castro, J. D. B., Potratz, J., Emerick, A. A., Pacheco, M. A. C. (2020).
789   Recent developments combining ensemble smoother and deep generative networks for
790   facies history matching. *Computational Geosciences*, *25*, 433-466.

Canchumuni, S. W. A., Emerick, A. A., Pacheco, M. A. C. (2019). Towards a robust parameterization for conditioning facies models using deep variational autoencoders and ensemble smoother. *Computers and Geosciences*, *128*, 87-102.

Chen, X., Hammond, G. E., Murray, C. J., Rockhold, M. L., Vermeul, V. R., Zachara, J. M. (2013). Application of ensemble-based data assimilation techniques for aquifer characterization using tracer data at Hanford 300 area. *Water Resources Research*, *49*(10), 7064-7076.

Chen, Y., Oliver, D. S. (2012). Ensemble randomized maximum likelihood method as an iterative ensemble smoother. *Mathematical Geosciences*, *44*, 1-26.

Chen, Y., Zhao, Z. (2020). Heat transfer in a 3D rough rock fracture with heterogeneous apertures. *International Journal of Rock Mechanics and Mining Sciences*, *134*, 104445.

Crestani, E., Camporese, M., Baú, D., Salandin, P. (2013). Ensemble Kalman filter versus ensemble smoother for assessing hydraulic conductivity via tracer test data assimilation. *Hydrology and Earth System Sciences*, *17*(4), 1517-1531.

Cui, T., Fox, C., O'Sullivan, M. J. (2011). Bayesian calibration of a large-scale geothermal reservoir model by a new adaptive delayed acceptance Metropolis Hastings algorithm. *Water Resources Research*, *47*, W10521.

Dorn, C., Linde, N., Borgne, T. L., Bour, O., de Dreuzy J. R. (2013). Conditioning of stochastic 3-D fracture networks to hydrological and geophysical data. *Advances in Water Resources*, *62*, 79-89.

Emerick, A. A., Reynolds, A. C. (2013). Ensemble smoother with multiple data assimilation. *Computers and Geosciences*, *55*, 3-15.

Evensen, G. (1994). Sequential data assimilation with a nonlinear quasi-geostrophic model using Monte Carlo methods to forecast error statistics. *Journal of Geophysical Research*, *99*, 10143-10162.

Evensen, G. (2018). Analysis of iterative ensemble smoothers for solving inverse problems. *Computational Geosciences*, *22*, 885-908.

Fienen, M. N., Luo, J., Kitanidis, P. K. (2006). A Bayesian geostatistical transfer function approach to tracer test analysis. *Water Resources Research*, *42*, W07426.

Fox, D. B., Koch, D. L., Tester, J. W. (2015). The effect of spatial aperture variations on the thermal performance of discretely fractured geothermal reservoirs. *Geothermal Energy*, *3*(1), 1-29.

Fu, P., Hao, Y., Walsh, S. D. C., Carrigan, C. R. (2016). Thermal drawdown-induced flow channeling in fractured geothermal reservoirs. *Rock Mechanics and Rock Engineering*, *49*(3), 1001-1024.

Guo, B., Fu, P., Hao, Y., Carrigan, C. R. (2016a). Investigating the possibility of using tracer tests for early identification of EGS reservoirs prone to flow channeling. 41st Workshop on Geothermal Reservoir Engineering, Stanford, CA.

Guo, B., Fu, P., Hao, Y., Peters, C. A., Carrigan, C. R. (2016b). Thermal drawdown-induced flow channeling in a single fracture in EGS. *Geothermics*, *61*, 46-62.

Hakim-Elahi, S., Jafarpour, B. (2017). A distance transform for continuous parameterization of discrete geologic facies for subsurface flow model calibration. *Water Resources Research*, *53*, 8226-8249.

Hawkins, A. J., Becker, M. W., Tester, J. W. (2018). Inert and adsorptive tracer tests for Field measurement of flow-wetted surface area. *Water Resources Research*, *54*, 5341-5358.

836 Hawkins, A. J., Fox, D. B., Matthew, M. W., Tester, J. W. (2017a). Measurement and simulation
837   of heat exchange in fractured bedrock using inert and thermally degrading tracers. *Water*
838   *Resources Research*, *53*, 1210-1230.
839 Hawkins, A. J., Becker, M. W., Tsoflias, G. P. (2017b) Evaluation of inert tracers in a bedrock
840   fracture using ground penetrating radar and thermal sensors. *Geothermics*, *67*, 86-94.
841 Hawkins, A. J., Fox, D. B., Koch, D. L., Becker, M. W., Tester, J. W. (2020). Predictive inverse
842   model for advective heat transfer in a short-circuited fracture: Dimensional analysis,
843   machine learning, and field demonstration. *Water Resources Research*,
844   *56*, e2020WR027065.
845 Hawkins, A. J., Bender, J. T., Grooms, R. D., Schissel, C. J., Tester, J. W. (2021). Temperature-
846   responsive smart tracers for field-measurement of inter-well thermal evolution:
847   Heterogeneous kinetics and field demonstration. *Geothermics*, *92*, 102046.
848 Irving, J., Singha, K. (2010). Stochastic inversion of tracer test and electrical geophysical data to
849   estimate hydraulic conductivities. *Water Resources Research*, *46*(11), W11514.
850 Jafarpour, B., McLaughlin, D. B. (2007). Efficient permeability parameterization with the
851   discrete cosine transform. SPE reservoir simulation symposium, Houston, Texas, USA.
852 Juliusson, E., Horne, R. N. (2013). Characterization of fractured reservoirs using tracer and flow-
853   rate data. *Water Resources Research*, *49*, 2327-2342.
854 Keller, J., Hendricks Franssen, H. J., Marquart, G. (2018). Comparing seven variants of the
855   ensemble Kalman filter: How many synthetic experiments are needed? *Water Resources*
856   *Research*, *54*, 6299-6318.
857 Kittilä, A., Jalali, M. R., Evans, K. F., Willmann, M., Saar, M. O., Kong, X. Z. (2019). Field
858   comparison of DNA-labeled nanoparticle and solute tracer transport in a fractured
859   crystalline rock. *Water Resources Research*, *55*(8), 6577-6595.
860 Laloy, E., Hérault, R., Jacques, D., Linde, N. (2018). Training-image based geostatistical
861   inversion using a spatial generative adversarial neural network. *Water Resources*
862   *Research*, *54*(1), 381-406.
863 Laloy, E., Hérault, R., Lee, J., Jacques, D., Linde, N. (2017). Inversion using a new low-
864   dimensional representation of complex binary geological media based on a deep neural
865   network. *Advances in Water Resources*, *110*, 387-405.
866 Liu, Y., Durlofsky, L. J. (2020). 3D CNN-PCA: A deep-learning-based parameterization for
867   complex geomodels. *Computers and Geosciences*, *148*, 104676.
868 Lochbühler, T., Pirot, G., Straubhaar, J., Linde, N. (2014). Conditioning of multiple-point
869   statistics facies simulations to tomographic images. *Mathematical Geosciences*, *46*, 625-
870   645.
871 Ma, X., Zhang, K., Yao, C., Zhang, L., Wang, J., Yang, Y., Yao, J. (2020). Multiscale-network
872   structure inversion of fractured media based on a hierarchical-parameterization and data-
873   driven evolutionary-optimization Method. *SPE Journal*, *25*(5), 2729-2748.
874 Maxwell, S. C., Rutledge, J., Jones, R., Fehler, M. (2010). Petroleum reservoir characterization
875   using downhole microseismic monitoring. *Geophysics*, *75(5)*, 75A129-75A137.
876 Mo, S., Zabaras, N., Shi, X., Wu, J. (2020). Integration of adversarial autoencoders with residual
877   dense convolutional networks for estimation of non-Gaussian hydraulic conductivities.
878   *Water Resources Research*, *56*(2), e2019WR026082..
879 Neuman, S. P. (2005). Trends, prospects and challenges in quantifying flow and transport
880   through fractured rocks. *Hydrogeology Journal*, *13*(1), 124-147.

881 Power, W. L., Tullis, T. E. (1992). The contact between opposing fault surfaces at Dixie Valley,
882   Nevada, and implications for fault mechanics. *Journal of Geophysical Research*, *97*,
883   15425-15435.

884 Pyrak-Nolte, L. J., Morris, J. P. (2000). Single fractures under normal stress: The relation
885   between fracture specific stiffness and fluid flow. *International Journal of Rock
886   Mechanics and Mining Sciences*, *37*, 245-262.

887 Radilla, G., Sausse, J., Sanjuan, B. & Fourar, M. (2012). Interpreting tracer tests in the enhanced
888   geothermal system (EGS) of Soultz-sous-Forêts using the equivalent stratified medium
889   approach. *Geothermics*, *44*, 43-51.

890 Sanjuan, B., Pinault, J. L., Rose, P., Gérard, A., Brach, M., Braibant, G., Crouzet, C., Foucher, J.
891   C., Gautier, A., Touzelet, S. (2006). Tracer testing of the geothermal heat exchanger at
892   Soultz-sous-Forêts (France) between 2000 and 2005. *Geothermics*, *35*, 622-653.

893 Sarma, P., Durlofsky, L. J., Aziz, K. (2008). Kernel principal component analysis for efficient
894   differentiable parameterization of multipoint geostatistics. *Mathematical Geosciences*,
895   *40*, 3-32.

896 Settgast, R. R., Fu, P., Walsh, S. D. C., White, J. A., Annavarapu, C., Ryerson, F. J. (2017). A
897   fully coupled method for massively parallel simulation of hydraulically driven fractures
898   in 3-dimensions. *International Journal for Numerical and Analytical Methods in
899   Geomechanics*, *41*, 627-653.

900 Shook, G. M. (2001). Predicting thermal breakthrough in heterogeneous media from tracer tests.
901   *Geothermics*, *30*, 573-589.

902 Shook, G.M. (2003). A simple, fast method of estimating fractured geometry from tracer tests.
903   *Geothermal Resources Council Transactions*, *27*, 407-411.

904 Shook, G. M., Suzuki, A. (2017). Use of tracers and temperature to estimate fracture surface area
905   for EGS reservoirs. *Geothermics*, *67*, 40-47.

906 Somogyvári, Y., Jalali, M., Jimenez Parras, S., Bayer, P. (2017). Synthetic fracture network
907   characterization with transdimensional inversion. *Water Resources Research*, *53*(6),
908   5104-5123.

909 Suzuki, A., Ikhwanda, F., Yamaguchi, A., Hashida, T. (2019). Estimations of fracture surface
910   area using tracer and temperature data in geothermal fields. *Geosciences*, *9*, 425.

911 Tang, H., Fu, P., Sherman, C. S., Zhang, J., Ju, X., Hamon, F., Azzolina, N. A., Burton-Kelly,
912   M., Morris, J. P. (2021). A deep learning-accelerated data assimilation and forecasting
913   workflow for commercial-scale geologic carbon storage. arXiv preprint: 2105.09468.

914 Tang, M., Liu, Y., Durlofsky, L. J. (2019). A deep-learning-based surrogate model for data
915   assimilation in dynamic subsurface flow problems. *Journal of Computational Physics*,
916   *413*, 109456.

917 Tian, W., Wu, X., Shen, T., Kalra, S. (2016). Estimation of hydraulic fracture volume utilizing
918   partitioning chemical tracer in shale gas formation. *Journal of Natural Gas Science and
919   Engineering*, *33*, 1069-1077.

920 van Leeuwen, P. J., Evensen, G. (1996). Data assimilation and inverse methods in terms of a
921   probabilistic formulation. *Monthly Weather Review*, *124*, 2898-2913.

922 Vo, H. X., Durlofsky, L. J. (2014). A new differentiable parameterization based on principal
923   component analysis for the low-dimensional representation of complex geological
924   models. *Mathematical Geosciences*, *46*(7), 775-813.

925   Vogt, C., Kosack, C., Marquart, G. (2012a). Stochastic inversion of the tracer experiment of the
926   enhanced geothermal system demonstration reservoir in Soultz-sous-Forêts — Revealing
927   pathways and estimating permeability distribution. *Geothermics*, *42*, 1-12.

928   Vogt, C., Marquart, G., Kosack, C., Wolf, A., Clauser, C. (2012b). Estimating the permeability
929   distribution and its uncertainty at the EGS demonstration reservoir Soultz-sous-Forêts
930   using the ensemble Kalman filter. *Water Resources Research*, *48*, W08517.

931   Vrugt, J. A. (2016). Markov chain Monte Carlo simulation using the DREAM software package:
932   Theory, concepts, and MATLAB implementation. *Environmental Modelling and
933   Software*, *75*, 273-316.

934   Wu, H., Fu, P., Morris, J. P., Mattson, E. D., Neupane, G., Smith, M. M., Hawkins, A. J., Zhang,
935   Y., Kneafsey, T., EGS Collab. (2021). Characterization of flow and transport in a fracture
936   network at the EGS Collab field experiment through stochastic modeling of tracer
937   recovery. *Journal of Hydrology*, *593*, 125888.

938   Wu, H., Fu, P., Morris, J. P. (2020). Predicting thermal responses at the EGS Collab testbed
939   based on tracer test-inferred flow fields. 45th Workshop on Geothermal Reservoir
940   Engineering, Stanford, CA..

941   Wu, H., Fu, P., Yang, X., Morris, J. P., Johnson, T. C., Settgast, R. R., Ryerson, F. J. (2019).
942   Accurate imaging of hydraulic fractures using templated electrical resistivity
943   tomography. *Geothermics*, *81*, 74-87.

944   Wu, X., Pope, G. A., Shook, G. M., Srinivasan, S. (2008). Prediction of enthalpy production
945   from fractured geothermal reservoirs using partitioning tracers. *International Journal of
946   Heat and Mass Transfer*, *51*, 1453-1466.

947   Zhang, J., Man, J., Lin, G., Wu, L., Zeng, L. (2018). Inverse modeling of hydrologic systems
948   with adaptive multifidelity Markov Chain Monte Carlo simulations. *Water Resources
949   Research*, *54*(7), 4867-4886.

950   Zhang, J., Zheng, Q., Wu, L., Zeng, L. (2020). Using deep learning to improve ensemble
951   smoother: Applications to subsurface characterization. *Water Resources Research*,
952   *56*, e2020WR027399.